

## $B \rightarrow K^* \tau \tau$ DECAY : USING MACHINE LEARNING TO SEPARATE SIGNAL FROM BACKGROUND

Author

QIXING DENG	CID: 02211125
YIDAN SUN	CID: 02208287
ZIYAO XIONG	CID: 02225789
JUNHUA YANG	CID: 02259287

Supervised by

DR HANAE TILQUIN

Assessed by

PROF MITESH PATEL

Abstract

This study investigates the rare decay  $B^0 \rightarrow K^{*0} \tau^+ \tau^-$ , which is sensitive to potential violations of lepton flavor universality predicted by the Standard Model. A Monte Carlo simulated dataset containing both signal and the dominant background process  $B^0 \rightarrow K^{*0} D^+ D^-$  was used to train and evaluate machine learning classifiers. After feature selection and parameter tuning, two supervised models—Boosted Decision Trees (BDTs) and Fully Connected Neural Networks (FCNNs)—were trained. Feature engineering was then applied to enhance classification performance. On the test set, the BDT achieved an AUC of  $0.912 \pm 0.000$  and an F1-score of  $0.828 \pm 0.001$ , while the FCNN reached an AUC of  $0.877 \pm 0.000$  and an F1-score of  $0.799 \pm 0.001$ . These results demonstrate that both models can robustly separate signal from background in rare decay searches, supporting their application in future LHCb analyses.

# CONTENTS

<b>Abstract</b>	<b>1</b>
<b>I Introduction and Motivation</b>	<b>3</b>
<b>II Theory</b>	<b>3</b>
A Signal and Background Decays	3
B Data Acquisition	4
1) LHCb Detector System	4
2) Monte Carlo Simulation	5
C Machine Learning Algorithms	5
1) Boosted Decision Tree	5
2) Fully Connected Neural Network	6
<b>III Method</b>	<b>7</b>
A Data Pre-processing	7
1) ID Selection	7
2) Class Balancing	7
3) Splitting Data	7
B Feature Selection	7
1) Irrelevant Features	7
2) Feature Correlation	8
3) Permutation Importance Analysis	8
C Parameter Study	9
1) BDT	9
2) Neural Network	10
<b>IV Findings with Raw Features</b>	<b>11</b>
A Explanation of Features	11
1) $B_0$ Mass	11
2) Vertex Fit Quality	12
3) Kinematics	12
B Model Performance	13
1) Choosing threshold Probability	13
2) Cross Validation and Confusion Matrices	13
<b>V Feature Engineering</b>	<b>14</b>
A $D, \tau$ Flying Distance	14
1) Computation	14
2) Discussions and Uncertainties	15
3) Further Combination	15
B Missing Mass and $Q^2$	15
1) Computation	15
2) Discussions and Uncertainties	16
C Frame Boosting	16
1) Computation	16
2) Discussions and Uncertainties	17
D Geometric Separation	18
1) Computation	18
2) Discussions and Uncertainties	18
<b>VI Results</b>	<b>18</b>
A Model Performance	18
B Feature Importance	20
C Evaluations	20
<b>VII Conclusion and Outlook</b>	<b>20</b>
<b>Appendix</b>	<b>22</b>

## I. INTRODUCTION AND MOTIVATION

Lepton Flavor Universality (LFU) is a fundamental feature of the Standard Model (SM), which posits that the electroweak gauge interactions couple equally to all three generations of charged leptons—electron ( $e$ ), muon ( $\mu$ ), and tau ( $\tau$ )—up to corrections arising from their mass differences [1]. This principle implies that, after accounting for phase space and kinematic effects, processes involving different lepton flavors should occur at the same rates. Deviations from LFU would therefore constitute clear evidence of physics beyond the SM.

In recent years, several measurements in  $B$  meson decays have hinted at such deviations, namely in the ratios

$$R_{D^{(*)}} = \frac{\mathcal{B}(B \rightarrow D^{(*)} \tau \nu)}{\mathcal{B}(B \rightarrow D^{(*)} \ell \nu)} \quad (\ell = e, \mu), \quad (1)$$

which exhibit deviations from SM predictions at nearly  $3\sigma$  level [2, 3, 4]. These tensions hint that NP, if present, may couple preferentially to third-generation leptons  $\tau$ .

Rare flavor-changing neutral current (FCNC) decays such as  $b \rightarrow s \tau^+ \tau^-$  are theoretically clean and highly sensitive to NP effects. In the SM, these processes occur only at the loop level, without any tree-level contributions. This loop suppression implies that any NP effect entering at tree level could lead to sizable deviations from the SM predictions, thereby enhancing the sensitivity to potential NP contributions. From the experimental side, the  $b \rightarrow s \tau^+ \tau^-$  channel is extremely challenging to access due to the presence of multiple neutrinos in  $\tau$  decays, which significantly reduces the reconstruction efficiency. However, this difficulty implies that any future observation of a signal in this channel would be less susceptible to systematic uncertainties or background misidentification, and thus highly indicative of genuine NP effects.

In the SM, the branching ratio of  $b \rightarrow s \tau^+ \tau^-$  is predicted to be at the level of  $\mathcal{O}(10^{-7})$  [5]. However, in several well-motivated NP scenarios, this decay can be significantly enhanced. For instance, models designed to explain the observed anomalies in  $R_{D^{(*)}}$  can simultaneously predict  $\mathcal{B}(B \rightarrow K^{(*)} \tau^+ \tau^-) \sim 10^{-4}$  [6], representing an enhancement of three orders of magnitude over the SM.

Nevertheless, among the various  $b \rightarrow s \tau^+ \tau^-$  transitions, the exclusive decay  $B^0 \rightarrow K^{*0} \tau^+ \tau^-$  stands out as an experimentally promising channel, particularly at the LHCb experiment. The  $K^{*0}$  meson decays promptly and cleanly into a pair of charged hadrons ( $K^- \pi^+$ ), which can be efficiently reconstructed with LHCb's forward geometry and excellent tracking resolution [7]. Compared to fully leptonic channels like  $B_s \rightarrow \tau^+ \tau^-$ , where both tau decays leave little visible information,  $B^0 \rightarrow K^{*0} \tau^+ \tau^-$  offers a favorable balance between theoretical cleanliness and experimental accessibility, making it a compelling target in the search for lepton flavor universality violation and other NP effects [8].

Despite its strong theoretical motivation, the decay  $B^0 \rightarrow K^{*0} \tau^+ \tau^-$  has not yet been observed experimentally. The most stringent constraint to date is an upper limit on the branching ratio,  $\mathcal{B}(B^0 \rightarrow K^{*0} \tau^+ \tau^-) < 3.1 \times 10^{-3}$  at 90% confidence level [9], which is still several orders of magnitude above the Standard Model expectation

and leaves significant room for potential new physics contributions.

One of the main challenges in future searches for  $B^0 \rightarrow K^{*0} \tau^+ \tau^-$  at LHCb lies in distinguishing this rare signal from overwhelming backgrounds. In particular, a highly problematic background arises from the decay  $B^0 \rightarrow K^{*0} D^+ D^-$ , whose visible final-state particles can be identical to those of the signal when both  $D$  mesons decay semileptonically.

In this study, we aim to develop a classification model that maximally discriminates between the  $B^0 \rightarrow K^{*0} \tau^+ \tau^-$  signal and the dominant  $B^0 \rightarrow K^{*0} D^+ D^-$  background. Our dataset consists of six Monte Carlo samples, simulating both signal and background processes, with a total of approximately 1 million events. Each event is characterized by 307 features, capturing detailed information about the dynamics, kinematics, and decay topology of the involved particles. Given the high dimensionality and the complex, non-linear correlations among variables, traditional statistical methods are inadequate for extracting the full discriminative power of the dataset. Machine learning techniques, particularly supervised classification models, provide a powerful alternative. These methods are capable of learning intricate patterns in the multi-dimensional feature space and can significantly enhance the signal-to-background separation. In what follows, we describe the design, training, and evaluation of machine learning classifiers aimed at identifying  $B^0 \rightarrow K^{*0} \tau^+ \tau^-$  events in the presence of challenging backgrounds.

## II. THEORY

### A. Signal and Background Decays

The signal decay under investigation is the rare process  $B^0 \rightarrow K^{*0} \tau^+ \tau^-$ , where the  $K^{*0}$  meson is an excited vector state of the  $K^0$  system, and it decays almost exclusively to  $K^- \pi^+$  through strong interactions [9]. Both  $\tau$  leptons decay leptonically into a muon and two neutrinos. As a result, the visible final-state particles are  $K^-, \pi^+, \mu^+$ , and  $\mu^-$ , accompanied by missing energy carried away by the neutrinos. The presence of the intermediate  $K^{*0}$  resonance provides a well-defined hadronic structure and enables more precise reconstruction of the decay kinematics.

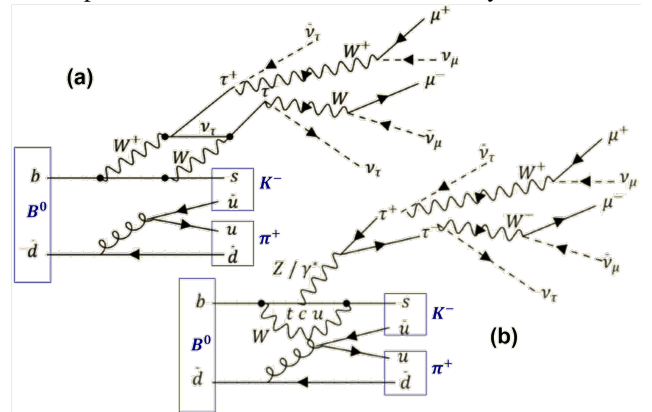


Figure 1: Feynman diagrams for the signal decay. Diagram (a) shows the box contribution involving virtual  $W$  bosons and neutrinos, while diagram (b) shows the penguin contribution mediated by loop-level exchange of virtual quarks and a  $Z/\gamma$  boson.

As shown in Fig. 1, the signal proceeds via a FCNC transition,  $b \rightarrow s\tau^+\tau^-$ , which is highly suppressed in the SM. Such FCNC processes can only occur via loop-level penguin or box diagrams.

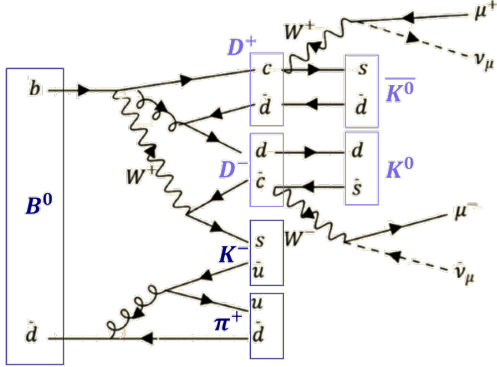


Figure 2: Quark-level Feynman diagram for the background process, where the  $B^0$  meson undergoes a tree-level  $b \rightarrow c\bar{s}$  transition.

A major background arises from the decay  $B^0 \rightarrow K^*D^+D^-$ , where both  $D^+$  and  $D^-$  mesons decay semileptonically via  $D \rightarrow K^0\mu\nu$ . This leads to the same visible final-state particles as in the signal process:  $K^-, \pi^+, \mu^+$ , and  $\mu^-$ . Crucially, this background originates from a  $b \rightarrow c\bar{s}$  transition, which proceeds via a tree-level diagram (as shown in Fig. 2) and therefore has a relatively large theoretical branching fraction of  $\mathcal{O}(10^{-4})$  [9], compared to that of the signal. As the visible final states are indistinguishable from those of the signal decay, this background presents a significant challenge for the analysis and must be carefully suppressed through kinematic and topological selection criteria.

It is also important to note that  $B^0$ - $\bar{B}^0$  mixing can occur before the decay, which effectively allows the meson to oscillate into its antiparticle. As a result, the charges of the final-state kaon and pion is reversed, yielding  $K^+\pi^-\mu^+\mu^-$ . Corresponding Feynman diagrams illustrating the  $\bar{B}^0$  decay are provided in Appendix A.

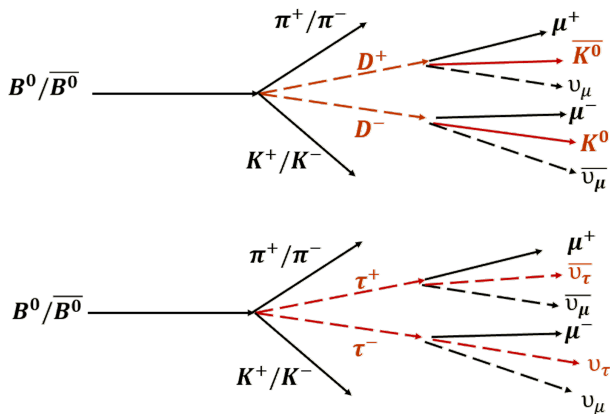


Figure 3: Diagrammatic comparison of the signal and main background decay chains. The major physical differences—such as intermediate states and decay products—are highlighted by the red lines.

A visual comparison of the signal and dominant background processes is shown in Fig. 3. The primary physical differences between the signal and background processes arise from the properties of their intermediate states. First,  $D$  mesons have a significantly longer lifetime than  $\tau$  leptons—approximately  $10^{-12}$  s compared to  $10^{-13}$  s—which allows them to travel further before decaying [2]. This results in a larger displacement between

the  $B^0$  decay vertex and the muon origin in background events. Second,  $D$  mesons (1.87 GeV) are more massive than  $\tau$  leptons (1.78 GeV) [9], and they decay into heavier particles, most notably the  $K^0$ , which is substantially heavier than the neutrinos produced in  $\tau \rightarrow \mu\nu\nu$ . This mass difference alters the kinematic distributions of the final-state muons. These differences in lifetime, mass, and decay product properties constitute the root physical distinctions between signal and background. They underpin all subsequent classification strategies.

## B. Data Acquisition

Our research is based on the simulated data replicating the conditions of the LHCb experiment at CERN. Since this decay,  $B^0 \rightarrow K^{*0}\tau^+\tau^-$ , has not yet been observed due to its extremely small predicted branching ratio in the SM, to study it, we use Monte Carlo (MC) simulations. The  $B^0$  meson is forced to decay exclusively via the target channel. This is implemented by assigning a 100% branching ratio to the desired mode while suppressing all others. While the overall decay spectrum is altered, the generated kinematic and angular distributions are consistent with those produced under LHCb detector conditions.

### 1) LHCb Detector System

At the LHC, two proton beams collide head-on along the  $z$ -axis [10]. In these proton-proton ( $pp$ ) collisions, bottom quark pairs ( $b\bar{b}$ ) are produced through high-energy interactions between their internal constituents (partons), and subsequently hadronize into  $B^0$  and  $\bar{B}^0$  mesons. Due to the unequal momentum fractions carried by the partons, the resulting mesons often acquire a net momentum along the beam ( $z$ ) axis [7].

The LHCb detector, a single-arm forward spectrometer covering the pseudorapidity range  $2 < \eta < 5$ , is designed to take advantage of this forward production [11]. Therefore, LHCb achieves high efficiency in detecting and reconstructing  $B$ -meson decays by covering the forward region where heavy-flavor hadrons are predominantly produced. Several key subsystems in LHCb enable the precise reconstruction of particle trajectories, decay vertices, and identities:

**Vertex Locator (VELO):** Positioned near the beamline, the VELO reconstructs the primary vertex (OWNPV) of the  $B^0$ , its decay vertex (ENDVERTEX), and the secondary vertices of  $D$  or  $\tau$  decays. These positions are crucial for determining the  $B^0$  flight direction and decay length.

**Dipole Magnet and Tracking Stations:** After leaving the VELO, charged particles enter a dipole magnet, which bends their paths due to the Lorentz force. The amount of curvature is proportional to the particle's momentum and charge. Tracking stations placed before and after the magnet allow reconstruction of the particle's momentum using the curvature of its trajectory:

$$p = qBR, \quad (2)$$

where  $p$  is momentum,  $q$  is electric charge,  $B$  is magnetic field strength, and  $R$  is the radius of curvature.

**Particle Identification:** Charged hadrons and muons are identified using the Ring Imaging Cherenkov (RICH) detectors and the muon system, respectively. The RICH detectors measure Cherenkov radiation emitted by charged

particles traveling faster than the speed of light in a given medium ( $v > c/n$ ), with the emission angle  $\theta_C$  given by  $\cos\theta_C = 1/(\beta n)$ , where  $\beta = v/c$  and  $n$  is the refractive index [12]. Since the particle momentum  $p$  is known from tracking, combining it with  $\beta$  extracted from  $\theta_C$  allows the particle mass to be inferred, enabling separation of pions, kaons, and protons. Muons, on the other hand, are identified by their ability to penetrate thick layers of absorber material and leave hits in downstream muon chambers [7]. The muon system provides high-purity muon identification, ensuring reliable reconstruction of muon kinematics for decays involving final-state muons.

In both the signal and background decays, only the charged kaon and pion from the  $K^{*0} \rightarrow K^+\pi^-$  decay, along with the two muons originating from the subsequent decays of  $\tau$  or  $D$  mesons, leave clean and reconstructable tracks in the detector. In contrast, intermediate resonances such as  $D^\pm$  and  $\tau^\pm$ , and neutral particles like  $K^0$  and neutrinos, decay too promptly or escape detection entirely. Consequently, the full decay topology must be inferred indirectly from the observable final-state particles and their kinematic and geometric correlations.

## 2) Monte Carlo Simulation

In addition to constraining the decay channel, Monte Carlo (MC) simulations provide ground-truth labels essential for supervised learning. The simulation pipeline closely mirrors the real LHCb data-taking process: proton-proton collisions are generated [13], heavy-flavor hadrons are produced and decayed into target final states such as  $B^0 \rightarrow K^{*0}\tau^+\tau^-$  and  $B^0 \rightarrow K^{*0}D^+D^-$ , with branching ratios set to 100% [14]. Particle interactions with the detector—such as ionization and scattering—are then simulated in detail, replicating the physical processes in the actual LHCb experiment. The resulting detector signals are processed using the same reconstruction algorithms as those applied to real LHCb data, producing high-level features like momenta, vertex displacements, and particle identification scores [15].

Each simulated event is labeled as either signal (true decay) or background (e.g., combinatorics or misreconstructed events), forming the dataset used to train classifiers such as Boosted Decision Trees or Neural Networks.

## C. Machine Learning Algorithms

Each Monte Carlo event in our classification task is labeled as signal (1) or background (0) and represented by features derived from reconstructed detector-level quantities. To learn the mapping from features to labels, we employ two supervised learning models widely used in high-energy physics: Boosted Decision Trees (BDTs) and Neural Networks (NNs). Both are effective in capturing non-linear correlations in high-dimensional spaces. Once trained, the models output a score between 0 and 1, interpreted as the signal probability. Applying a threshold to this score enables signal-background separation. We train the BDT and NN independently on the same dataset and compare their performance using standard classification metrics.

### 1) Boosted Decision Tree

A decision tree is a predictive model that partitions the feature space through a series of binary splits based on feature thresholds. Each input ends in a terminal node, or *leaf*, which assigns a prediction value.

Boosted Decision Trees (BDTs) combine multiple shallow decision trees, or weak learners, into a strong classifier by iteratively minimizing classification error, as illustrated in Fig. 4. In each iteration, a new tree is trained to correct the residuals of the current ensemble by minimizing an objective function that balances training loss and model complexity [16]:

$$\mathcal{L}^{(t)} = \sum_{i=1}^n l(y_i, \hat{y}_i^{(t-1)} + f_t(x_i)) + \Omega(f_t), \quad (3)$$

where  $l(y_i, \hat{y}_i)$  is a loss function that measures the discrepancy between the true label  $y_i$  and the predicted output  $\hat{y}_i$ , and  $\Omega(f_t)$  is a regularization term that penalizes the complexity of the newly added tree  $f_t$ .

The loss function used for this training is the binary cross-entropy loss [16]:

$$l(y_i, \hat{y}_i) = -[y_i \log(\hat{y}_i) + (1 - y_i) \log(1 - \hat{y}_i)], \quad (4)$$

where the predicted probability  $\hat{y}_i \in (0, 1)$  is obtained by applying a sigmoid transformation to a real-valued score  $z_i$ :

$$\sigma(z_i) = \frac{1}{1 + e^{-z_i}}. \quad (5)$$

This maps unbounded model outputs to the unit interval, enabling probabilistic interpretation in the classification.

The regularization term  $\Omega(f)$  controls overfitting by penalizing overly complex trees, and is defined as [16]:

$$\Omega(f) = \gamma T + \frac{1}{2} \lambda \sum_{j=1}^T w_j^2 + \alpha \sum_{j=1}^T |w_j|, \quad (6)$$

where  $T$  is the number of leaves in the tree,  $\gamma$  controls the penalty for adding new leaves.  $\lambda$  and  $\alpha$  are the regularization strengths for L2 and L1 penalties, respectively. The L2 term imposes a quadratic penalty that encourages smaller weights and improves numerical stability. The L1 term promotes sparsity by driving less informative weights to zero, effectively performing automatic feature selection. This formulation encourages the model to generalize well while accurately capturing nonlinear patterns in the data.

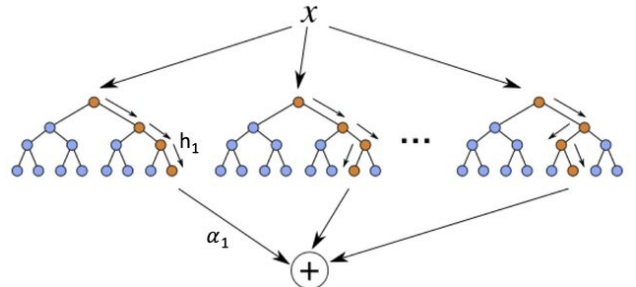


Figure 4: Illustration of a Boosted Decision Tree (BDT) model. Multiple shallow decision trees are sequentially trained, each correcting the residual errors of the previous ensemble. Their outputs are combined, typically through a weighted sum, to form a strong classifier. Adapted from Ref. [17].

While the binary cross-entropy (logloss) is used as the primary loss function during model training due to its differentiability and compatibility with gradient-based optimization, the area under the ROC curve (AUC) is often

simultaneously monitored as an evaluation metric.

The Receiver Operating Characteristic (ROC) curve is a graphical representation of a classifier's diagnostic ability as its discrimination threshold is varied. It is particularly informative for binary classification problems. The ROC curve plots:

True Positive Rate (TPR or Recall) on the Y-axis:

$$\text{TPR} = \frac{TP}{TP + FN} \quad (7)$$

False Positive Rate (FPR) on the X-axis:

$$\text{FPR} = \frac{FP}{FP + TN}, \quad (8)$$

where  $TP$  (True Positives) refers to signal events correctly predicted as signal;  $TN$  (True Negatives) refers to background events correctly predicted as background;  $FP$  (False Positives) refers to background events incorrectly predicted as signal;  $FN$  (False Negatives) refers to signal events incorrectly predicted as background.

The Area Under the Curve (AUC) represents the integral of the Receiver Operating Characteristic (ROC) curve. It is computed as:

$$\text{AUC} = \int_0^1 \text{TPR}(\text{FPR}) d(\text{FPR}). \quad (9)$$

AUC quantifies the model's ability to distinguish between signal and background, independent of the classification threshold. An AUC value closer to 1.0 indicates stronger discriminative performance, while a value near 0.5 suggests random guessing.

## 2) Fully Connected Neural Network

In this task, we use fully connected neural networks (FCNNs), which are well suited for structured, high-level features in LHCb data. Unlike CNNs or RNNs, which exploit spatial or temporal patterns, FCNNs are ideal for processing flat feature vectors common in particle physics classification tasks.

FCNN is a versatile machine learning model inspired by the structure and function of biological neural systems in the brains of animals. The basic unit of a neural network is called a neuron. A single neuron can be considered as a system that performs a linear operation followed by a non-linear transformation [18]. Specifically, each neuron receives a set of input values  $\mathbf{X}$ , applies a linear transformation through weights  $\mathbf{W}$ , adds a bias  $b$ , and then passes the result through a non-linear activation function. The activation function determines whether and to what extent the neuron becomes active, introducing non-linearity that allows the network to model complex relationships. Mathematically, the output of a neuron is given by [18]:

$$y = \sigma(\mathbf{W} \cdot \mathbf{X} + b), \quad (10)$$

where  $\sigma$  is the activation function. Intuitively, the weights control how strongly each input feature contributes to the neuron's output, while the bias shifts the activation threshold.

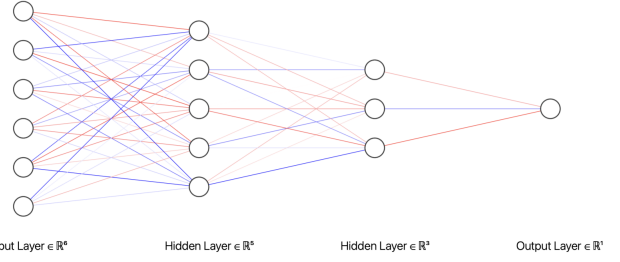


Figure 5: Example feedforward neural network architecture. Each node represents a neuron, and each edge corresponds to a trainable weight. Red and blue indicate positive and negative weights, respectively, with transparency indicating magnitude.

The network is organized into layers, as shown in Fig 5. The input layer receives the features of each event; one or more hidden layers perform intermediate transformations; and the final output layer produces a score used for classification. Each hidden layer applies the Rectified Linear Unit (ReLU) activation function [19],

$$\text{ReLU}(x) = \max(0, x), \quad (11)$$

which introduces non-linearity by allowing only positive activations to propagate forward.

The output layer uses a sigmoid activation (Eq. 5) to produce a continuous score in the range  $(0, 1)$ , interpretable as the probability that the event is signal.

The network is trained by minimizing the following objective function [20]:

$$\mathcal{L}_{\text{total}} = \frac{1}{N} \sum_{i=1}^N \ell(y_i, \hat{y}_i) + \lambda \mathcal{R}(\Theta), \quad (12)$$

where  $\ell(y_i, \hat{y}_i)$  is the binary cross-entropy loss defined in Eq. 4, and  $\mathcal{R}(\Theta)$  denotes the L2 norm of the model parameters  $\Theta = \{\mathbf{W}^{(l)}, b^{(l)}\}$ , applied across all layers. The regularization coefficient  $\lambda$  controls the strength of this penalty and plays a similar role to the regularization parameter used in the BDT model, balancing data fitting with model complexity.

While L1 regularization was used in the BDT model to encourage sparsity in feature usage, we do not apply it here, as neural networks typically benefit from smooth weight distributions rather than sparse connectivity. L2 regularization thus provides a more suitable inductive bias for this architecture.

In gradient-based optimization, each parameter  $\theta$  is updated iteratively in the direction that reduces the loss function, using the gradient of the loss with respect to  $\theta$ . In this study, all weights and biases in the network are optimized using the Adam optimizer, which computes individual, adaptive learning rates for each parameter. The parameter update rule at iteration  $t$  is [21]:

$$\theta_{t+1} = \theta_t - \eta \cdot \frac{\hat{m}_t}{\sqrt{\hat{v}_t + \epsilon}}, \quad (13)$$

where  $\eta$  is the base learning rate,  $\hat{m}_t$  and  $\hat{v}_t$  are bias-corrected estimates of the gradient and the squared gradient, and  $\epsilon$  is a small constant added for numerical stability. This adaptive mechanism allows Adam to converge faster and more reliably, especially in high-dimensional parameter spaces.

### III. METHOD

#### A. Data Pre-processing

##### 1) ID Selection

In the Monte Carlo simulation, particle ID scores (e.g., ProbNNmu, ProbNNk) are derived from pre-trained classifiers using track-level features like momentum and energy deposition. These scores reflect the likelihood that a track corresponds to a specific particle type, such as a muon, kaon, or pion.

However, PID scores are probabilistic and subject to uncertainties. For instance, high-momentum pions may have muon-like trajectories, leading to erroneously high ProbNNmu scores. This causes the reconstructed muon kinematics to actually reflect pion behavior, introducing inconsistencies in kinematic variables.

To address this, we applied a truth-level filter before training, only retaining candidates whose TrueID matches the expected particle type. These IDs follow the Monte Carlo numbering scheme, where each particle species is associated with a unique ID (e.g., 211 for  $\pi^+$ , 321 for  $K^+$ ) [22]. It ensures that training is based on correctly identified particles and not affected by PID misassignments.

It is also crucial to ensure that selected particles originate from the correct decay chain. For example, kaons or pions arising from undesired resonances like  $\rho$  or  $\phi$ , rather than from  $K^{*0}$  or  $B^0$ , introduce label noise that can degrade classifier performance.

To prevent such contamination, we applied ancestry-based filtering by requiring specific MotherID values. Kaons and pions must originate from a  $K^{*0}$  or directly from a  $B^0$ , while signal muons must stem from  $\tau$  decays and background muons from charm (D) mesons. This ensures that only final-state particles consistent with the target decay processes are used, improving model robustness and generalizability.

After applying these selections, only about 25% of the original events remain, reflecting substantial contamination from misidentified or misattributed tracks. This underscores the importance of truth-level filtering in constructing a clean and physically meaningful training dataset.

##### 2) Class Balancing

In the filtered dataset, background events outnumber signal events by roughly 3:1. This class imbalance can bias the model toward the majority class. To mitigate this, we applied either class weighting to emphasize the minority class during training, or undersampling to reduce the number of background events to balance the classes.

Specifically, class weights are incorporated into the loss function to penalize misclassifications of the minority class (signal events) more heavily. Without weighting, the model tends to favor the majority class, as this minimizes the overall (unweighted) loss. This yields a weighted binary cross-entropy loss function, defined as:

$$\mathcal{L}_{\text{weighted}} = -[w_1 \cdot y \cdot \log(\hat{y}) + w_0 \cdot (1 - y) \cdot \log(1 - \hat{y})] \quad (14)$$

where  $y \in \{0, 1\}$  is the true label (1 for signal, 0 for background), and  $\hat{y} \in (0, 1)$  is the predicted probability from

the sigmoid output. The weights  $w_1$  and  $w_0$  correspond to the signal and background classes, respectively.

The class weights are computed based on the inverse class frequencies, using the formula:

$$w_c = \frac{N}{K \cdot N_c} \quad (15)$$

where  $N$  is the total number of events in the dataset,  $K = 2$  is the number of classes (signal and background), and  $N_c$  is the number of samples in class  $c \in \{0, 1\}$ . This weighting scheme ensures that the minority class has a proportionally greater influence during training. While straightforward to implement, it can lead to optimization instability—most notably, overfitting to the minority class. In such cases, the model may misclassify many background events as signal in an attempt to minimize the weighted loss.

An alternative strategy is random undersampling, which reduces the number of background events to balance the class distribution. This can improve sensitivity to the signal by mitigating redundancy in the majority class. However, it may also discard informative background examples, potentially limiting model generalization.

##### 3) Splitting Data

After constructing a class-balanced dataset, it is split into training, validation, and test sets. The model learns from the training set by updating its parameters to minimize classification loss. The validation set is used to monitor overfitting and tune hyperparameters, ensuring generalization to unseen data [23]. The test set remains unseen during training to avoid data leakage and provide an unbiased estimate of model performance.

This study uses three years of data organized into six file sets, each containing one signal and one background dataset. Four sets were combined and randomly split into training and validation sets (80:20), while the remaining two sets were used as the test set.

#### B. Feature Selection

##### 1) Irrelevant Features

Among the 307 available features, we applied a feature selection procedure to exclude variables that are irrelevant or potentially harmful to classification.

**Detector-related metadata** such as eventNumber, runNumber, and polarity reflect experimental conditions rather than physics content. For example, polarity encodes the LHCb magnet orientation, which is periodically reversed to reduce detector-induced asymmetries [7]. Including such features risks introducing spurious correlations tied to data-taking configurations.

**Raw vertex coordinates** like \_ENDVERTEX\_Y and \_OWNPV\_Z represent absolute positions of production and decay vertices. Although useful for geometric calculations, their event-to-event fluctuations add noise without providing consistent discriminative power.

**Monte Carlo truth labels** (e.g., \_TRUEID, MOTHER\_ID) are only available in simulated data. Using them during training would lead to information leakage and undermine the model's applicability to real data.

**Low-variance features** were excluded by computing the normalized variance of each standardized feature and removing those below a 0.01 threshold. These included

constant or nearly constant quantities such as invariant particle masses and certain PID scores that show minimal variation across the dataset and therefore offer no discriminative power.

After filtering, 155 features were retained for training.

## 2) Feature Correlation

Highly correlated features add redundant data, slowing training and increasing overfitting risk. They also skew feature-importance scores—correlated variables compete for attribution—making model interpretation unreliable. We computed pairwise correlations and drop highly redundant features. The Pearson correlation coefficient between two features are obtained by

$$r_{XY} = \frac{\sum_{i=1}^n (X_i - \bar{X})(Y_i - \bar{Y})}{(n-1)\sigma_X\sigma_Y}, \quad (16)$$

where  $\bar{X}$  and  $\bar{Y}$  are the sample means, and  $\sigma_X$ ,  $\sigma_Y$  are the sample standard deviations of  $X$  and  $Y$ , respectively.

Fig. 6 presents the correlation network among the kinematic variables. Each connected pair or cluster of nodes represents a group of features with a Pearson correlation coefficient above 0.99 (i.e.,  $r \approx 1$ ), indicating near-redundancy. It is observed that the momentum  $P$ , longitudinal momentum  $PZ$ , and energy  $PE$  of particles often exhibit strong correlations. This is expected, as LHCb boosts particles predominantly along the  $z$ -axis, as discussed in Section II B 1). Similarly, the energy and momentum of the same particle are often highly correlated due to the relativistic relation  $E^2 = p^2 + m^2$ , where  $m$  is the particle mass. AtVertex P(momentum at the reconstructed decay vertex) also exhibit perfect correlation with  $P$ , as both are derived from the same fitted track parameters. To avoid redundancy, only one variable was retained from each such correlated cluster. We adopted a priority order of  $P > PE > PZ > AtvertexP$ , as  $P$  is a directly measured scalar quantity that offers stable resolution and broad applicability, while  $E$  is typically reconstructed and may be affected by uncertainties in mass assignment or calorimeter response.

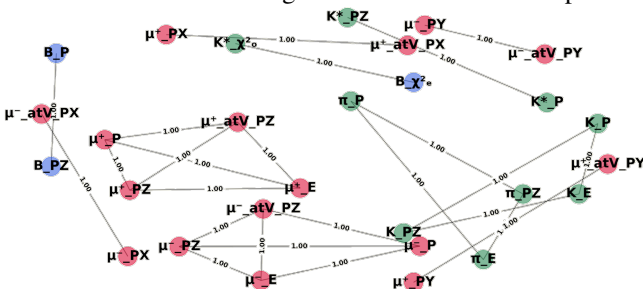


Figure 6: Correlation network among momentum and energy-related variables. Red, green, and blue nodes represent features associated with muons,  $B^0$ , and kaons, respectively.

Furthermore, although not shown in Fig. 6, PID features computed from different versions of the same algorithm—such as `pion_MC15TuneV1_ProbNNpi` and `pion_ProbNNpi`, exhibit correlations close to unity. This is expected, as they are based on the same detector inputs and produced by similarly trained classification models [5]. In this case, we retained the standard version (e.g., `pion_ProbNNpi`) over tune-specific alternatives.

## 3) Permutation Importance Analysis

Using all 97 features can cause overfitting and slow training, so we ran permutation importance to select the most impactful ones. We then trained a depth-five BDT and a two-layer FCNN with minimal tuning to focus on robust, generalizable predictors.

Permutation importance was calculated by shuffling each feature and measuring the resulting drop in AUC and log-loss; these threshold-independent scores were then used to rank all 97 features by their impact on model performance.

We retrained each model on progressively larger subsets of top-ranked features, recording AUC and log-loss as shown in Fig. 7. Once these curves plateau—identifying the feature count that maximizes AUC and minimizes log-loss—we select that number as optimal, since adding more features yields no further performance gain.

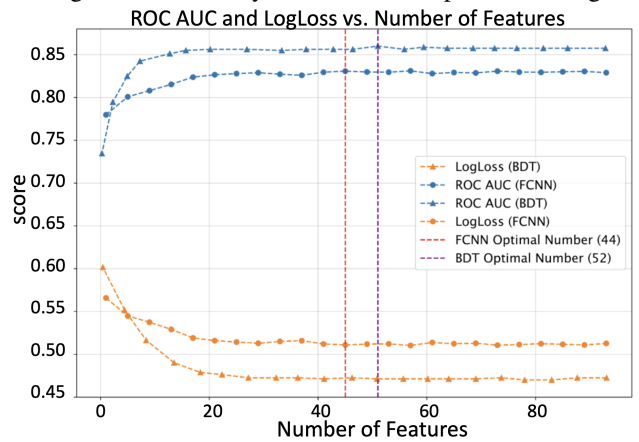


Figure 7: Variation of ROC AUC and LogLoss with the number of input features for both BDT and FCNN models. The performance stabilizes as more features are included. The optimal number of features is marked by dashed vertical lines.

The optimal feature counts are similar between the two models, with 52 features for BDT and 44 for FCNN out of a total of 97. This suggests that both models are able to capture the relevant information from the data using a comparable number of features. The consistency further implies that the two models rely on similar feature patterns, despite being based on fundamentally different learning architectures. To examine the dependence on features in each model in more details, top five important features were studied, as shown in Fig. 8. The high consistency in feature dependency in BDT and FCNN can be seen from their shared top 2 important features, which are `B0_M` and `B0_ENDVERTEX_CHI2`. These two features also show a much higher importance scores ( $\gtrsim 0.1$ ) compared to the rest of the features ( $< 0.04$  in BDT and  $\approx 0.01$  in FCNN), which further indicates their significance.

BDT's top-5 features all score higher under permutation importance than the FCNN's (Fig. 8) because BDTs explicitly split on individual variables—shuffling a key feature directly degrades its performance. FCNNs, however, learn via weighted combinations across layers, so perturbing a single input has a more diffuse effect. Since permutation importance only measures each feature's marginal impact, it naturally favors models (like BDTs) that rely on individual splits.

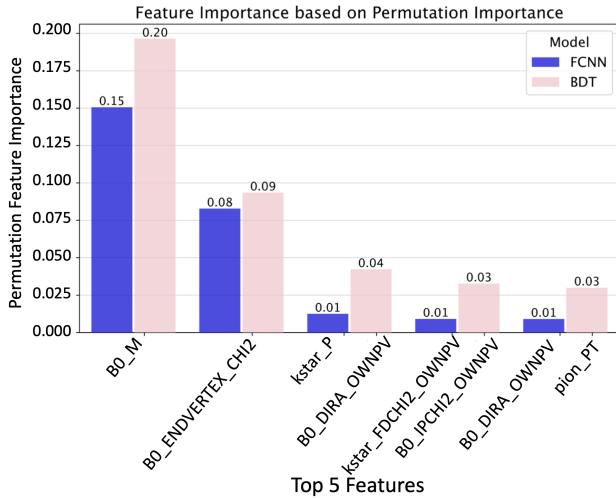


Figure 8: Top 5 original features ranked by permutation importance for both FCNN and BDT models.

### C. Parameter Study

We then tuned each model’s hyperparameters, configuration variables that govern the training behavior and model capacity, to capture complex patterns and mitigate overfitting. Overfitting occurs when a model performs well on the training data but fails to generalize to new, unseen data, often due to excessively fitting noise or specific fluctuations in the training set.

We first evaluated hyperparameter tuning for both BDT and FCNN under the two class imbalance strategies introduced in Section III B 2): random undersampling and class weight adjustment. Baseline tests showed that random undersampling boosted AUC by about 15% over class-weighting, so it is used as the default preprocessing step.

#### 1) BDT

We focused initially on `max_depth` and `learning_rate`, which are known to exert the most significant influence on model complexity and overall performances, while keeping all other parameters at their default values. The `max_depth` sets the maximum depth of each decision tree. Deeper trees capture more complex feature interactions but risk overfitting, while shallow trees may underfit by missing key patterns. The `learning_rate` scales the contribution of each new tree. Lower values promote stable learning and better generalization, though requiring more trees. Higher values speed up training but increase overfitting risk.

By jointly optimizing `max_depth` and `learning_rate`, we aimed to achieve a balance between model expressiveness and generalization. The results of the grid search are presented in Fig. 9, which visualizes the AUC scores over the parameter space, and Fig. 10, which provides a detailed view of the AUC trends with respect to `learning_rate` under different `max_depth` settings.

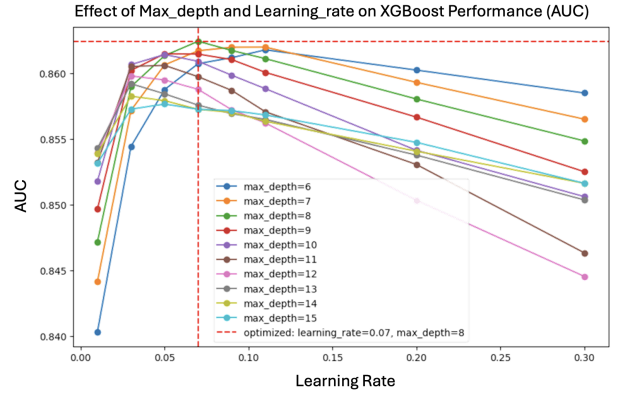


Figure 10: Line plot illustrating the impact of `learning_rate` on ROC AUC performance under different `max_depth` settings in the XGBoost model. Each curve corresponds to a fixed `max_depth`, and the AUC is evaluated. A peak is observed around `learning_rate = 0.07` and `max_depth = 8`, indicated by the red dashed lines, representing the optimal combination of the two hyperparameters found in this grid search.

Effect of Max\_depth and Learning\_rate on XGBoost Performance (AUC)

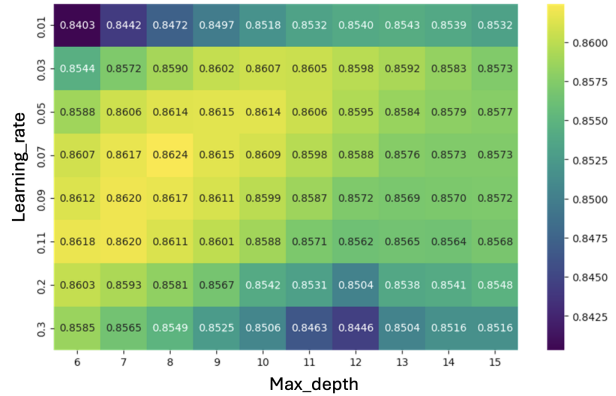


Figure 9: Grid search result showing the impact of `max_depth` and `learning_rate` on the performance (ROC AUC) of the XGBoost model. Each cell represents the AUC score obtained for a specific combination of hyperparameters. Higher AUC values are concentrated around intermediate values of `max_depth` (6–8) and moderate `learning_rate` (0.05–0.1).

The optimal combination was observed at `max_depth = 8` and `learning_rate = 0.07`, which yields the highest average AUC score of 0.8624. This setting provides sufficient model complexity to capture non-linear interactions among the 52 input features, while the moderately low learning rate ensures stable and gradual convergence. We conducted further hyperparameter tuning with values of these two parameters fixed and the search results are illustrated in Appendix B.

We first explored the effect of randomness control parameters, namely `subsample` and `colsample_bytree`. These parameters determine the fraction of training samples and input features randomly selected during each boosting round, respectively. The best performance was achieved when both `subsample` and `colsample_bytree` were set to 1.0, suggesting the model benefits from utilizing the full training data and feature set in each round. The large dataset size likely provides sufficient diversity and robustness against overfitting, making aggressive subsampling unnecessary. Furthermore, the fact that no performance gain was observed through feature subsampling indicates that most of the selected features are informative, highlighting the effectiveness of our feature

selection process.

To further improve model generalization and prevent overfitting, we conducted a grid search over the regularization hyperparameters of the XGBoost model: `reg_lambda` (L2 regularization) and `reg_alpha` (L1 regularization), as defined in Eq. 6. The model performance remained relatively stable across a range of regularization values, but a clear improvement was observed at higher `reg_alpha` settings. The highest AUC was achieved at `reg_lambda = 0.1` and `reg_alpha = 10`, meaning a combination of modest L2 regularization and strong L1 regularization is beneficial in our setting. With 52 features, the L1 penalty removes weak or redundant variables and improves robustness, demonstrating that regularization can still enhance performance by controlling model complexity even after feature selection.

In the final hyperparameter sweep, we focused on two XGBoost settings that govern tree complexity: `min_child_weight` and `gamma`. The former sets the minimum sum of instance weights (Hessians) required to form a child node, with lower values allowing deeper, more flexible splits at the risk of overfitting. The latter defines the minimum loss reduction needed to perform a split, so higher `gamma` values discourage marginal splits and produce simpler trees.

The best AUC was achieved with `min_child_weight=1` and `gamma=0.01`. Increasing `gamma` steadily reduces AUC, indicating underfitting from over-pruning, and larger `min_child_weight` values also slightly impair performance. These results show that our dataset benefits from deep, finely split trees and that aggressive regularization is unnecessary given the robustness of the selected features.

## 2) Neural Network

We tuned the FCNN architecture—layers, neurons per layer, and activation—and optimizer settings, specifically the learning rate and L2 weight\_decay.

The `learning_rate` parameter determines the step size for each update in the model’s weights during optimisation. A too large learning rate would cause the model to oscillate or fail to converge, while a too one might get stuck in a local minimum. Hence finding an optimal learning rate is essential for the model to converge effectively and stably.

The FCNN depth controls its capacity for hierarchical feature learning. Deeper networks can capture more complex patterns but induce higher overfitting risk and require longer training times. With a moderate input dimensionality of 44 features, we therefore focused on architectures with 2–3 hidden layers.

The number of neurons per hidden layer sets the network’s width and its capacity to encode features. Increasing neurons allows richer representations but raises overfitting risk and computational cost.

To analyse the trade-off between a wide (shallow network with many neurons per layer) and a deep neural network (few neurons but many layers) with appropriate learning rate, a shallower FCNN with 2 layers with neuron numbers of 16, 32, 64, 128, and 256 was investigated first. These values were chosen to be powers of 2 for efficient memory management in

modern computer architectures [24]. Parameter study on 2-layer model is shown in Fig. 11, where ROC AUC scores were used for comparing the model performance, with higher AUC indicating better performance.

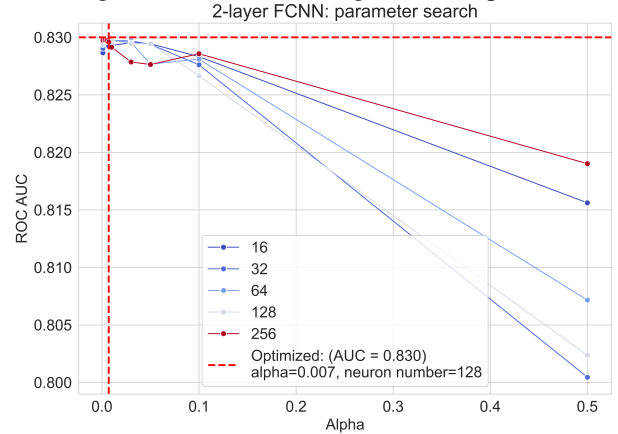


Figure 11: Hyperparameter tuning results for the 2-layer FCNN model, showing ROC AUC scores as a function of regularization strength (alpha) across different hidden layer sizes. The best hyperparameters are alpha = 0.007 and 128 neurons in hidden layer.

For the 2-layer FCNN, the optimal configuration used 128 neurons and a learning rate of 0.007. Scanning  $\alpha$  from 0.001 to 0.5 showed that layers with 256 neurons achieved higher AUC at the lowest ( $\leq 0.003$ ) and highest ( $> 0.1$ )  $\alpha$  values, reflecting overfitting in the former case and unstable training in the latter, while performance declined at intermediate  $\alpha$ . This outcome motivated a corresponding hyperparameter search on a 3-layer FCNN (see Fig. 12).

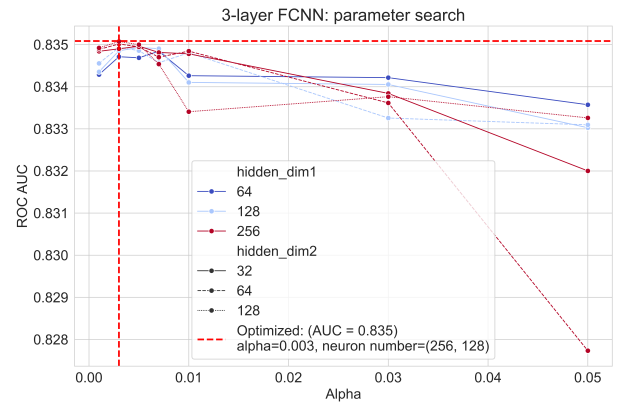


Figure 12: Hyperparameter tuning results for the 3-layer FCNN model, showing ROC AUC as a function of the regularization strength (alpha) across different neuron configurations. The best hyperparameters are alpha = 0.003 and using 256 and 128 in first and second hidden layers.

The 3-layer FCNN achieved an AUC of 0.835, compared to 0.830 for the 2-layer model. Its optimal configuration uses two hidden layers of 258 and 128 neurons with a learning rate of 0.003. The added depth and width enable the network to extract more sophisticated feature representations.

Activation functions such as ReLU and LeakyReLU were compared under the same optimal hyperparameters, but AUC remained virtually unchanged. We therefore adopted ReLU for hidden layers and a final Sigmoid activation to normalize the output to [0,1] for probability estimation.

L2 regularization was evaluated by varying the `weight_decay` parameter, but AUC remained essentially unchanged. This suggests the FCNN’s architecture already

balances capacity and generalization effectively, making L2 penalties largely redundant. We therefore adopted `weight_decay=0.01` as the optimal value.

## IV. FINDINGS WITH RAW FEATURES

### A. Explanation of Features

Among the selected features for both BDT and FCNN, the majority (over 70%) are composite in nature. These include features associated with reconstructed particles such as the  $B^0$  (from all four decay products),  $J/\psi$  (from  $\mu^+\mu^-$ ), and  $K^*$  (from  $K^\pm\pi^\mp$ ). This can inform future feature engineering efforts by highlighting the effectiveness of composite features.

#### 1) $B^0$ Mass

Among all input features, both the BDT and neural network rank `B0_M` as the most important variable, as shown in Fig. 8. This feature is computed from the four-momenta of its visible decay products: a kaon, a pion, and two muons. Since the  $B^0$  meson decays before detection, its momentum and energy cannot be measured directly. Instead, `B0_M` is reconstructed using the following invariant mass formula:

$$M_{B^0} = \sqrt{\left(\sum_{i \in \{K^\pm, \pi^\mp, \mu^+, \mu^-\}} E_i\right)^2 - \left\|\sum_{i \in \{K^\pm, \pi^\mp, \mu^+, \mu^-\}} \vec{p}_i\right\|^2}, \quad (17)$$

which can be expanded to:

$$M_{B^0}^2 = \sum_i m_i^2 + 2 \sum_{i < j} (E_i E_j - \vec{p}_i \cdot \vec{p}_j) \quad (18)$$

where it introduces cross terms of energy and momentum. To explain the observed differences in the reconstructed  $B^0$  mass from visible decay products, we analyze each contributing term in Eq. 18 separately. Since both the signal and background processes involve the same set of visible particles ( $K^\pm, \pi^\mp, \mu^+, \mu^-$ ), the visible mass term remains identical for both decays. However, the nature of the invisible decay products differs significantly between the two reactions: the signal decay involves four neutrinos, whereas the background decay includes two neutrinos and two additional neutral kaons ( $K^0$ ).

Due to energy conservation, the presence of the more massive  $K^0$  mesons in the background channel leads to a substantial share of the total energy being carried away by the invisible system. As a result, the visible system in background events receives less energy compared to that in signal events. This difference directly affects the energy-dependent cross term in Eq. 18, making it larger for signal events.

In addition, the invariant mass of the intermediate  $D^\pm$  meson in the background decay ( $m_{D^\pm} \approx 1.870 \text{ GeV}/c^2$ ) is slightly higher than that of the  $\tau^\pm$  lepton in the signal decay ( $m_{\tau^\pm} \approx 1.777 \text{ GeV}/c^2$ ) [9]. As a result, in the  $B^0/\bar{B}^0$  rest frame, the  $D^\pm$  carries less momentum and has a lower velocity than the  $\tau^\pm$ . According to Eq. 19, this leads to a smaller angle  $\theta$  between the momentum of the  $D^\pm$  and the  $B^0/\bar{B}^0$  direction in background events:

$$\tan \theta = \frac{u' \sin \theta'}{\gamma(v_B + u' \cos \theta')}. \quad (19)$$

This expression results from a Lorentz transformation between the  $B^0$  rest frame and the lab frame, where the

$B^0$  is boosted along the  $z$ -axis with a Lorentz factor  $\gamma$ . In Eq. 19,  $\theta'$  and  $\theta$  denote the angle between the intermediate particle's momentum and the  $z$ -axis in the  $B^0$  rest frame and the lab frame, respectively. The quantities  $u'$  and  $v_B$  represent the velocity of the intermediate particle in the  $B^0$  rest frame and the velocity of the  $B^0$  meson in the lab frame.

Since the  $B^0$  rest frame is isotropic, the angle  $\theta'$  is uniformly distributed in the absence of spin correlations. Therefore, differences in the observed lab-frame angle  $\theta$  arise solely from differences in the boost parameters, such as the intermediate particle's velocity  $u'$ , and reflect the degree of angular collimation induced by the Lorentz boost.

In the limit of small  $u'$ , such as that associated with the heavier intermediate  $D^\pm$  meson, the angle  $\theta$  remains small. This implies that the momentum of the intermediate particle is closely aligned with the  $B^0$  flight direction. As a result, the decay products of  $D^\pm$  (e.g.,  $\pi^\pm$  and  $K^\mp$ ) emerge in the lab frame with broader angular distributions relative to the  $z$ -axis, further influencing the observed decay topology.

In both signal and background processes, the kaon and pion are produced alongside either a  $\tau^\pm$  or a  $D^\pm$  meson in the  $B^0$  decay. Due to the broader angular distribution of the  $\tau^\pm$  momentum in the  $B^0$  rest frame, the visible system in the signal decay experiences weaker kinematic constraints from momentum conservation. This allows the kaon and pion to emerge at wider angles with respect to the  $B^0$  flight direction, resulting in a less collimated configuration.

As a consequence, the scalar products  $\vec{p}_i \cdot \vec{p}_j$  between visible particles, appearing in the cross-term of Eq. 18, become smaller in signal events. This reduces the magnitude of the total three-momentum of the visible system, thereby lowering the reconstructed  $B^0$  mass.

The same reasoning applies to the invisible components of the decay. In the signal process, the four neutrinos originating from  $\tau^\pm$  decay are emitted more isotropically, leading to smaller mutual scalar products and weaker momentum alignment with the visible system. In contrast, the background decay includes two neutrinos and two  $K^0$  mesons, where the more massive  $K^0$  particles tend to carry momentum along more defined directions. This difference further enhances the contrast in the energy-momentum structure between signal and background.

Therefore, the signal decay yields a higher and broader range for the reconstructed invariant mass. The result is shown in the histogram in Fig. 13. As expected, signal events have a higher median mass (2589.99 MeV) and broader spread, with an interquartile range (IQR) of about 618.62 MeV, compared to background events which exhibit a lower median (2229.38 MeV) and narrower IQR (531.50 MeV).

While the reconstructed mass `B0_M` should in principle never exceed the physical mass of the  $B^0$  meson (5279.65 MeV), due to missing energy carried away by invisible particles, a small number of events in both signal and background exceed this theoretical bound. Specifically, we observe 0.12% such events in the signal sample and 0.10% in the background. These unphysical values likely arise from imperfections in the Monte Carlo reconstruction pipeline, including track misassignment, vertex fitting instabilities, or kinematic overestimation during simulation. Although the fraction is small, they highlight the need

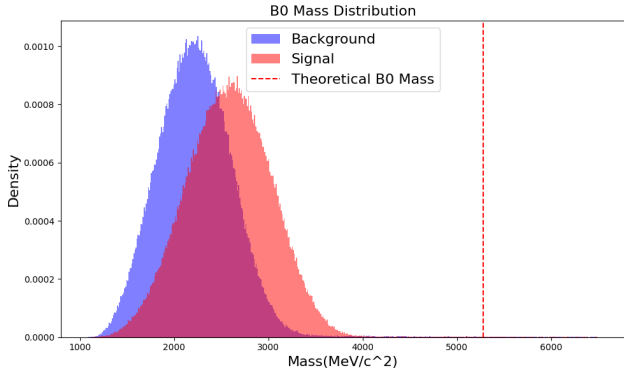


Figure 13: Distribution of the reconstructed invariant mass  $B_0$  for signal and background events. The red dashed line marks the theoretical  $B^0$  mass ( $5279.65 \text{ MeV}/c^2$ ), which should not be exceeded in the presence of missing neutrinos. A small fraction of events in both samples violate this bound, likely due to reconstruction artifacts in the Monte Carlo simulation.

for careful treatment of high-mass tails when interpreting model predictions.

### 2) Vertex Fit Quality

The variable  $B_0\_ENDVERTEX\_CHI2$  measures the quality of the vertex fit associated with the reconstructed  $B^0$  meson decay. In high-energy physics analyses, a vertex fit attempts to determine the point in space where all decay product tracks intersect, under the assumption that they originate from a common parent particle. The fit quality is quantified using the chi-squared statistic:

$$\chi^2 = \sum_i \frac{(x_i - x_{\text{fit}})^2}{\sigma_i^2}, \quad (20)$$

where  $x_i$  represents the measured parameters (typically positions or directions) of the  $i^{\text{th}}$  track,  $x_{\text{fit}}$  is the best-fit vertex value, and  $\sigma_i$  is the measurement uncertainty. This chi-squared value is dimensionless and reflects both the spatial convergence and consistency of the decay products' tracks.

Physically, the end vertex marks the decay point of the  $B^0$  meson. In signal events, the decay is prompt, with muons originating via short-lived  $\tau$  leptons, leading to tightly clustered tracks and low values of  $B_0\_ENDVERTEX\_CHI2$ . In contrast, background events involve long-lived  $D^\pm$  mesons that decay at displaced vertices. The resulting muons introduce spatial spread in the reconstructed tracks, degrading the vertex fit and yielding higher  $\chi^2$  values, as shown in Fig. 14.

Similarly to  $B_0\_ENDVERTEX\_CHI2$ , the top-ranked features in both the NN and BDT models include several vertex-related quantities that reflect the spatial reconstruction quality of the  $B^0$  decay. For instance,  $B_0\_IPCHI2\_OWNPV$  and  $B_0\_FDCHI2\_OWNPV$  quantify the impact parameter significance and the flight distance significance of the  $B^0$  with respect to its associated primary vertex (PV). These are defined as

$$IP\chi^2 = \frac{d_{\text{IP}}^2}{\sigma_d^2}, \quad FD\chi^2 = \frac{d_{\text{FD}}^2}{\sigma_{\text{FD}}^2}, \quad (21)$$

where  $d_{\text{IP}}$  and  $d_{\text{FD}}$  are the measured distances, and  $\sigma$  the associated uncertainties. Signal events tend to have larger flight distance significance ( $\uparrow 9.0\%$ ) but smaller impact parameter significance ( $\downarrow 15.3\%$ ), indicating a more accurately reconstructed and more prompt  $B^0$  decay vertex.

Another geometric variable,  $B_0\_DIRA\_OWNPV$ , measures

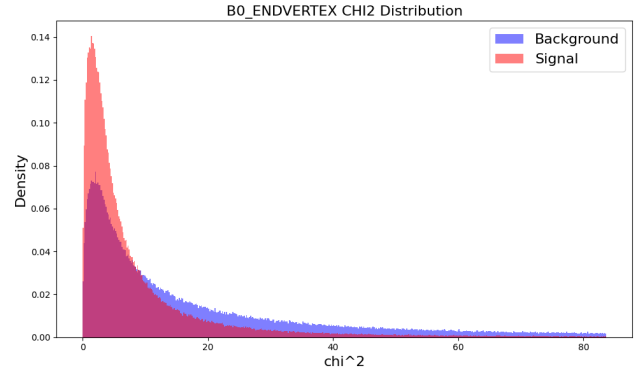


Figure 14: Distribution of the vertex fit quality variable  $B_0\_ENDVERTEX\_CHI2$ . Signal events exhibit lower  $\chi^2$  values, reflecting well-reconstructed decay vertices. In contrast, background events show a longer tail due to poorer vertex consistency. This variable is dimensionless and provides strong discrimination power between the two classes.

the cosine of the angle between the reconstructed momentum of the  $B^0$  and the displacement vector from the PV to its decay vertex. Signal events show slightly smaller DIRA values, consistent with a broader angular separation of the decay products caused by the presence of intermediate  $\tau$  leptons. A similar behavior is observed in  $kstar\_FDCHI2\_OWNPV$ , where signal events exhibit higher vertex significance ( $\uparrow 15.7\%$ ), reflecting a more collimated and well-defined  $K^*$  decay geometry.

### 3) Kinematics

While momentum and energy of individual particles are certainly fundamental observables, they do not appear highly ranked in feature importance. This is because classification performance relies more on composite features that capture correlations between particles (e.g., invariant mass and vertex  $\chi^2$ ), which summarize multiple aspects of the event into a single quantity that better reflects the global event topology.

Among the few individual kinematic variables that rank highly in importance is the transverse momentum of the pion ( $p_{\text{ion\_PT}}$ ). The median value of this feature is noticeably higher in the signal sample ( $1153.6 \text{ MeV}/c$ ) than in the background ( $1033.7 \text{ MeV}/c$ ), corresponding to an increase of approximately 11.6%. Since  $p_T$  measures momentum perpendicular to the beam axis, it is particularly sensitive to the spatial distribution of the particles in the transverse plane. In signal decays, the lighter intermediate  $\tau$  and multiple neutrinos introduce more randomness in the final-state kinematics, leading to increased transverse activity.

Another top-ranked kinematic feature is the total momentum of the reconstructed  $K^*$  resonance ( $kstar\_P$ ), which combines the momenta of the kaon and pion from the  $B^0$  decay. The median  $K^*$  momentum is slightly higher in the signal ( $33856.8 \text{ MeV}/c$ ) than in the background ( $33547.5 \text{ MeV}/c$ ), corresponding to an increase of approximately 0.92%. This modest but consistent difference reflects the fact that background events involve two massive  $D^\pm$  mesons, which carry away more of the  $B^0$  energy.

Notably, all transverse momentum ( $P_T$ ) and total momentum ( $P$ ) features were retained in the selected feature list, whereas only three individual  $P_X$  or  $P_Y$  components were selected. This suggests that analyzing transverse

momentum as a whole is more informative than considering its Cartesian components separately.

## B. Model Performance

### 1) Choosing threshold Probability

Although our training data have been reweighted to achieve an approximately balanced signal-to-background ratio, the true event distribution in LHCb is highly imbalanced, with signal events being much rarer than background. In this context, it is important to interpret evaluation metrics carefully.

In binary classification tasks, machine learning models typically output probability scores between 0 and 1. To assign class labels, a decision threshold must first be selected. Once the threshold is chosen, performance can be evaluated using threshold-dependent metrics such as *accuracy*, *precision*, *recall*, and the *F1-score*. These metrics reflect different aspects of classification quality. In addition, threshold-independent metrics such as the area under the ROC curve (AUC) are also commonly reported to assess the model’s overall discriminative ability. The ROC curve of two models are provided in Appendix F.

Accuracy measures the overall proportion of correctly classified events. However, in class-imbalanced settings, it can be misleading, as it may be dominated by the majority class. For example, a classifier that always predicts background may still achieve high accuracy if signal events are rare. Precision and recall provide more informative insights in such cases: precision quantifies the proportion of predicted signal events that are truly signal, while recall measures the fraction of actual signal events that are correctly identified. The F1-score combines both as their harmonic mean:

$$F1 = 2 \cdot \frac{\text{Precision} \cdot \text{Recall}}{\text{Precision} + \text{Recall}}. \quad (22)$$

To ensure a balanced trade-off between identifying as many true signal events as possible and maintaining the reliability of predicted signal events, we optimized the classification threshold based on the F1-score. This metric is particularly suitable in our context, where both high recall and high precision are essential. We selected the thresholds that maximize the F1-score on the validation set: 0.406 for the BDT and 0.410 for the FCNN, as illustrated in Figure 15.

The optimal thresholds are both below the default value of 0.5, which indicates that the classifiers assign moderately conservative scores to signal events. This behavior suggests that the signal and background score distributions exhibit partial overlap, a consequence of both the inherent class imbalance and the limited separability in the feature space. As a result, a lower threshold is required to maximize the F1-score by recovering more true positives while controlling false positives.

### 2) Cross Validation and Confusion Matrices

To quantify the potential fluctuations in performance metrics that arise from the arbitrary selection of training and test datasets, we applied K-fold cross-validation in our model evaluation process. Specifically, the dataset was stochastically partitioned into 5 subsets. The model is subsequently trained 5 times, with each iteration using one of the subsets as the validation set and the remaining four subsets as the training set. This approach results in 5

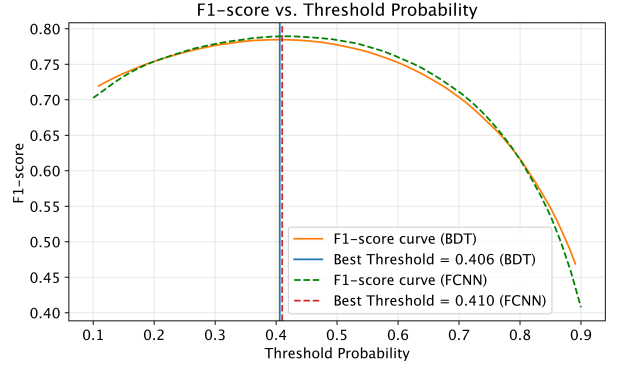


Figure 15: F1-score optimization curves for the BDT and FCNN models. The classification thresholds corresponding to the maximum F1-scores are 0.406 for the BDT and 0.410 for the FCNN.

distinct sets of performance metrics, from which the mean and standard deviation can be computed:

Table 1: COMPARISON OF CLASSIFICATION METRICS: FCNN VS. BDT

Metric	FCNN	BDT
Accuracy	0.740 ± 0.001	0.780 ± 0.002
Precision	0.700 ± 0.001	0.740 ± 0.002
Recall	0.834 ± 0.001	0.840 ± 0.003
F1-score	0.761 ± 0.001	0.780 ± 0.001
ROC AUC	0.841 ± 0.000	0.860 ± 0.000

The mean values represent the average performance across different data splits, while the standard deviations reflect the degree of random error in the model’s performance. Accordingly, the low variability in the metrics suggests stable classification performance. Both the BDT and FCNN models demonstrate strong

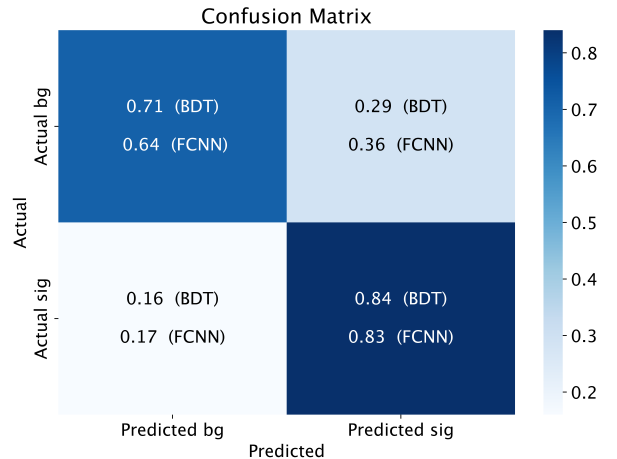


Figure 16: Normalized confusion matrices for the BDT and FCNN models at their respective optimal F1-score thresholds. Each cell shows the fraction of events in a true class (rows) that are predicted as a certain class (columns), with rows normalized to sum to 1. The diagonal elements represent correct classifications, while off-diagonal elements correspond to misclassifications.

classification performance in distinguishing signal from background events. Notably, both models achieve high recall—0.840 for BDT and 0.834 for FCNN—indicating their effectiveness in recovering a large fraction of true signal events. The F1-scores of 0.780 (BDT) and 0.761

(FCNN), which harmonize precision and recall, further confirm that both models maintain a balanced trade-off between signal recovery and prediction reliability.

The close agreement in recall and F1-score across two structurally different models—tree-based and neural network-based—suggests that the essential discriminative patterns in the current feature space have been effectively captured.

However, subtle differences remain. The BDT model attains higher precision (0.740 vs. 0.700) and overall accuracy (0.780 vs. 0.740), implying a stronger ability to reject background events and reduce false positives, while maintaining high signal efficiency. The confusion matrix confirms this: compared to the FCNN, the BDT misclassifies fewer background events as signal. These differences likely stem from the BDT’s ability to model sharp, axis-aligned decision boundaries and exploit hierarchical feature splits, which can more effectively isolate background-dominated regions in the feature space.

To further reduce false positives while preserving sensitivity to signal, future work could focus on designing higher-level, physics-inspired features. Improvements in feature quality may lead to performance gains that go beyond what can be achieved by tuning the model architecture alone.

## V. FEATURE ENGINEERING

Throughout the feature engineering process, we apply the Kolmogorov–Smirnov (KS) test as a diagnostic tool to quantify how well a newly constructed feature separates signal from background. The KS test, which quantifies the maximum difference between the empirical cumulative distribution functions (ECDFs) of two samples. The corresponding test statistic is defined as:

$$D = \sup_x |F_1(x) - F_2(x)|, \quad (23)$$

where  $F_1(x)$  and  $F_2(x)$  are the ECDFs of the signal and background samples, respectively. A larger  $D$  indicates greater divergence between the two distributions, and the corresponding  $p$ -value quantifies the statistical significance of this difference.

### A. $D, \tau$ Flying Distance

#### 1) Computation

Since both background and signal events have the same parent particles,  $B^0/\bar{B}^0$ , and final decay products, a primary physical difference between background and signal events is their intermediate states:  $D^\pm$  mesons for background reaction and  $\tau^\pm$  leptons for signal reaction. Hence, the physical quantities of these two states would provide useful information for classification. One of the quantities discussed and quantified in this paper is their flying distance (fd), which is the distance travelled by the  $D^\pm$  and  $\tau^\pm$ , estimated using two intersection points, as shown in Fig.17. The first intersection point, which is the end vertex of  $B^0/\bar{B}^0$ , denoted as  $r_{B^0\text{end}}$ , corresponds to the decay of the  $B^0/\bar{B}^0$ . The second intersection point is unknown but could be computed from the reconstruction of the trajectories of the  $B^0/\bar{B}^0$  and the  $\mu^\pm$ .

The trajectories of the  $B^0/\bar{B}^0$  can be expressed using  $r_{B^0\text{end}}$  and its travel direction, which is along the

axis  $r_{B^0\text{end}} - r_{B^0\text{own}}$ , where  $r_{B^0\text{own}}$  is where it was generated. For  $\mu^\pm$ , their trajectories are expressed with their reference vertices and momentum, represented by  $r_{\mu\text{own}}$  and  $\vec{p}_\mu$ . Eq.24 shows how this intersection point could be represented,

$$r_{B^0\text{end}} + \lambda_1 \Delta r_{B^0} = r_{\mu^-} + \lambda_2 p_{\mu^-}, \quad (24)$$

where  $\Delta r_{B^0} = r_{B^0\text{end}} - r_{B^0\text{own}}$ , and  $\lambda_1, \lambda_2$  are unknowns to be determined. The left and right side of the equation is the intersection point computed using the trajectory of  $B^0$  and  $\mu^-$  respectively. Provided three equations and two unknowns, as expressed in Eq.25, we applied the least squared method to estimate the intersection point by minimizing the distance between two trajectories.

$$\begin{bmatrix} \Delta r_{x,B^0} - p_{x,\mu\text{ref}} \\ \Delta r_{y,B^0} - p_{y,\mu\text{ref}} \\ \Delta r_{z,B^0} - p_{z,\mu\text{ref}} \end{bmatrix} \begin{bmatrix} \lambda_1 \\ \lambda_2 \end{bmatrix} = \begin{bmatrix} r_{x,\mu\text{ref}} - r_{x,B^0\text{end}} \\ r_{y,\mu\text{ref}} - r_{y,B^0\text{end}} \\ r_{z,\mu\text{ref}} - r_{z,B^0\text{end}} \end{bmatrix} \quad (25)$$

The mid-point of two possible intersection points that gave the shortest distance was used in flying distance calculation. The distribution in Fig.18 shows the estimated flying distances of  $D^-$  for background and  $\tau^-$  for signal.

The two distributions are clearly distinct. As expected,

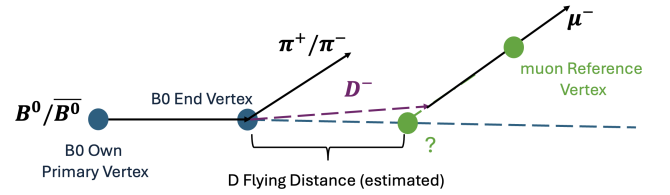


Figure 17: Part of the decay process for background reactions, where  $B^0/\bar{B}^0$  has  $D^-$  as an intermediate state before decaying into  $\mu^-$ . The purple line shows that the actual flight distance of  $D^-$  may not align with the  $B^0/\bar{B}^0$  axis.

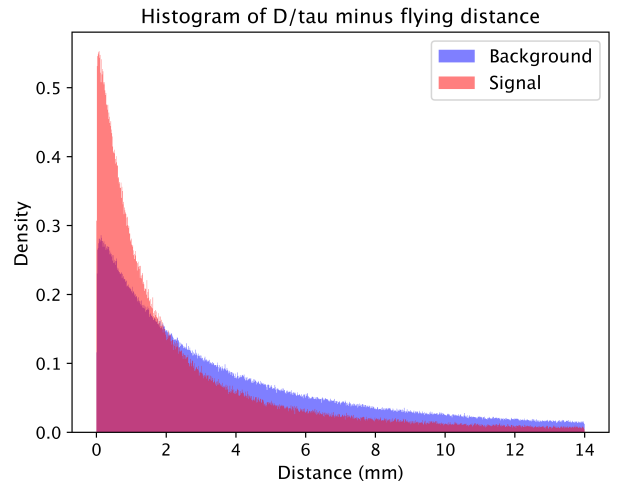


Figure 18: Distribution of flight distances for  $D^-$  (background events) and for  $\mu^-$  (signal events).

the mean flying distance of  $D^-$  was higher than  $\tau^-$ , with 5.21mm compared to 2.12mm. Since the flying distance of intermediate states was considered as the lab-frame decay length,

$$\text{fd} = \beta \gamma c \tau = \frac{p}{m} c \tau, \quad (26)$$

which comes from multiplying the particle’s time-dilated lifetime  $\gamma \tau$  by its velocity  $\beta c$ . Although the  $\tau^-$  may have higher momentum than the  $D^-$ , its proper lifetime is

approximately three times shorter. This dominates over the momentum, hence smaller flying distance in  $D^-$ .

### 2) Discussions and Uncertainties

There were several error sources in the computation of flying distances, the most significant being the uncertainty in the intersection point. In addition to uncertainties arising from its estimation, the vertex position uncertainties of the  $B^0/\bar{B}^0$  mesons ( $\vec{r}_{B^0\_end}$  and  $\vec{r}_{B^0\_own}$ ) were also included in the error propagation. These uncertainties stem from limitations in the reconstruction of the  $B^0/\bar{B}^0$  trajectories in the dataset. The distribution of relative uncertainties in flying distance is shown in Fig. 34 in Appendix C. A threshold of 5% relative error was chosen to compare the two classes: 4.22% of the signal events (flying distance of  $\tau$ ) and 3.81% of the background events (flying distance of  $D^-$ ) exhibited percentage errors greater than 5%.

The slightly higher percentage error in  $\tau$  indicates the misalignment problem. In the computation, the flying direction of the intermediate state was assumed to align exactly with the travel direction of the parent  $B^0/\bar{B}^0$ , as illustrated in Fig.17. This approximation holds more accurately for  $D^-$  than for  $\tau^-$  since the heavier  $D^-$  tends to be more collimated along the  $B^0/\bar{B}^0$  flight axis due to its lower velocity in the rest frame.

### 3) Further Combination

Due to charge-parity symmetry, we expect the theoretical distributions of the flying distances for  $D^\pm$  pairs and  $\tau^\pm$  pairs to be the same [25]. However, with various estimations made during the computation and the measurement errors from the dataset itself, we observed a slight difference between the flying distance distribution for the intermediate particles with opposite charges. The  $\tau^-$  distribution shows a mean of 5.84mm compared to 5.96mm in the  $\tau^+$  distribution; and the  $D^-$  shows a mean value of 9.92mm compared with 10.00mm in  $D^+$ . Hence, two flying distance features of  $D^\pm$  could be combined into a single feature of  $D$ , and the same applied for  $\tau$ . This combination could be done in various ways, including using the mean, the maximum value, or the minimum value in two sets of data. These new features are named as `fd_max`, `fd_min`, or `fd_mean`. Histograms of these combined features are shown in Appendix C.

We also performed Kolmogorov–Smirnov (KS) tests to quantify the distributional differences between signal and background events for each flying distance variable, both before and after combining the opposite-charge particle pairs. The results are shown in Table 2. All the combined

Table 2: KS STATISTICS IN FLYING DISTANCES (FD) BEFORE AND AFTER COMBINATIONS

Feature	KS statistic
fd plus ( $D^+/\tau^+$ )	0.2114
fd minus ( $D^-/\tau^-$ )	0.2111
fd mean	0.2439
fd max	0.2408
fd min	0.2129

features show an increase in KS statistics compared with the

flying distance of the single charged particles. We expect this greater distinction between signal and background classes would further optimize the model’s performance.

## B. Missing Mass and $Q^2$

### 1) Computation

As discussed in Section IV A 1), the presence of invisible decay products leads to missing momentum and energy, so the reconstructed  $B^0$  four-momentum based solely on visible particles is inherently inaccurate. To estimate the full four-momentum of the  $B^0$  meson in the presence of missing energy from invisible decay products, we adopted a mass-scaling approximation that corrects the longitudinal momentum  $p_z$  of the visible decay system, where the corrected longitudinal momentum is given by  $p_{z,B^0} = p_{z,vis} \times \frac{m_{B^0}}{m_{vis}}$ . This approach relies on the fact that the  $B^0$  meson is primarily boosted along the beam (z) axis in a hadron collider environment.

From the computation of flying distance, we recognized that the  $B^0$  flies in the direction  $\Delta\vec{r}_{B^0}$ . Let  $\hat{r}$  denote the normalized flight direction from  $r_{B^0\_end}$  to  $r_{B^0\_own}$ . Since the corrected longitudinal momentum  $p_{z,B^0}$  is known and the z-component of  $\hat{r}$  is  $\hat{r}_z$ , the total momentum magnitude is given by  $|\vec{p}_{B^0}| = p_{z,B^0}/\hat{r}_z$ . The transverse momentum components are then reconstructed according to  $p_{x,B^0} = |\vec{p}_{B^0}| \cdot \hat{r}_x$  and  $p_{y,B^0} = |\vec{p}_{B^0}| \cdot \hat{r}_y$ .

The corrected energy was computed via the relativistic energy-momentum relation:

$$E_{B^0} = \sqrt{|\vec{p}_{B^0}|^2 + m_{B^0}^2}. \quad (27)$$

Using this corrected four-momentum ( $E_{B^0}, \vec{p}_{B^0}$ ), we computed the missing mass  $M_{miss}$  as the Lorentz-invariant difference between the corrected and visible four-momenta:

$$M_{missing} = \sqrt{(\Delta E)^2 - \|\Delta\vec{P}\|^2}, \quad (28)$$

where

$$\begin{aligned} \Delta E &= E_{B^0,corr} - (E_{\mu^+} + E_{\mu^-} + E_K + E_\pi) \\ \Delta\vec{P} &= \vec{p}_{B^0,corr} - (\vec{p}_{\mu^+} + \vec{p}_{\mu^-} + \vec{p}_K + \vec{p}_\pi), \end{aligned} \quad (29)$$

in which, energy and momentum of visible particles ( $\mu^+$ ,  $\mu^-$ ,  $K^+$  or  $K^-$ ,  $\pi^+$  or  $\pi^-$ ) are subtracted. This variable effectively captures the energy carried away by all invisible particles.

In background events, the missing system consists of two  $K^0$  mesons and two neutrinos. Following the same logic as Eq. 17 and Eq. 18, the missing mass squared is given by:

$$M_{miss}^2 = 2m_{K^0}^2 + 2 \sum_{i<j} (E_i E_j - \vec{p}_i \cdot \vec{p}_j), \quad (30)$$

where the sum runs over all pairs of missing particles, and  $\theta_{ij}$  is the angle between the momenta of particles  $i$  and  $j$ . The first term reflects the intrinsic masses of the missing  $K^0$  mesons, while the second term accounts for the non-collinearity among the missing particles. Thus, the missing mass distribution is expected to start around  $\sqrt{2} \times m_{K^0} \approx 703 \text{ MeV}$  [9].

In signal events, the missing system consists of four neutrinos, each approximately massless. The missing mass squared is then given by:

$$M_{miss}^2 = 2 \sum_{i<j} (E_i E_j - \vec{p}_i \cdot \vec{p}_j), \quad (31)$$

since neutrino is assumed to be massless. Therefore, the missing mass arises purely from the angular spread between the neutrinos. In the idealized case where all neutrinos are emitted collinearly, the missing mass would be exactly zero. Consequently, the observed missing mass in background events is generally larger than in signal events, as the presence of two massive  $K^0$  mesons contributes a significant intrinsic mass to the missing system, while in signal events the missing mass arises only from the finite opening angles between nearly massless neutrinos, as shown in Fig. 19.

In addition to the missing mass, the properties of the intermediate states—specifically the  $\tau^+\tau^-$  system in the signal and the  $D^+D^-$  system in the background—are also crucial for distinguishing different processes. These intermediate states are invisible in the detector, but their missing mass squared, often referred to as the squared momentum transfer  $q^2$  in flavor physics, provides valuable information about the event. The calculation follows:

$$q^2 = \left( E_{B^0, \text{corr}} - \sum_i E_i \right)^2 - \left\| \vec{P}_{B^0, \text{corr}} - \sum_i \vec{P}_i \right\|^2, \quad (32)$$

where the sum runs over all visible final-state particles  $i \in \{\mu^+, \mu^-, K, \pi\}$ .

Similar to Eq. 30 and Eq. 31, the starting point of the background  $q^2$  distribution corresponds to  $2m_D^2$ , where  $m_D \approx 1869 \text{ MeV}/c^2$ , resulting in a starting value of approximately  $7.0 \times 10^6 \text{ MeV}^2/c^4$  [9]. For the signal, the starting point corresponds to  $2m_\tau^2$ , with  $m_\tau \approx 1777 \text{ MeV}/c^2$ , giving a starting value of approximately  $6.3 \times 10^6 \text{ MeV}^2/c^4$  [9].

For signal events involving  $\tau^+\tau^-$ , the  $q^2$  distribution tends to peak at lower values, due to the lighter intrinsic mass of the intermediate particles, as shown in Fig. 20. This confirms the strong discriminating power of both variables.

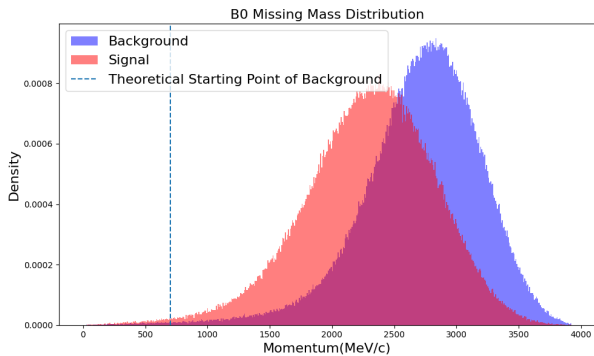


Figure 19: Missing mass distribution for signal and background events, with the vertical line indicating the theoretical threshold.

## 2) Discussions and Uncertainties

As shown in Fig. 19, approximately 0.307% of background events exhibit missing mass values below the expected kinematic threshold, indicating physical inconsistencies. Additionally, 2.154% of background events yield undefined (NaN) missing mass values, corresponding to cases where negative values arise in the calculation of  $E^2 - p^2$ . Similarly, 0.89% of background events and 0.56% of signal events show  $q^2$  values below their respective theoretical starting points. These non-physical or abnormal values reflect sources of error inherent in our calculation.

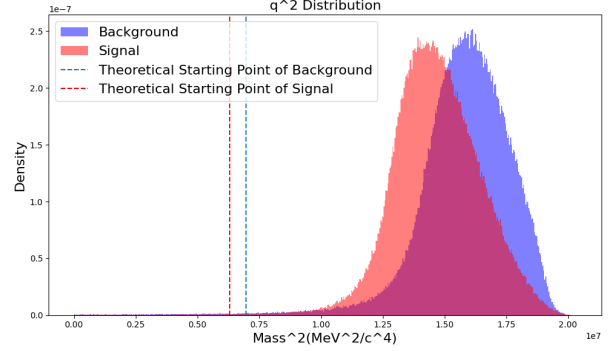


Figure 20:  $q^2$  distribution for signal and background events, with vertical lines indicating theoretical thresholds.

The first source of error is the reconstruction uncertainty in the  $B^0$  decay and production vertices ( $r_{B^0, \text{end}} - r_{B^0, \text{own}}$ ), as discussed in Section V A 2). All reconstructed momenta and energies of invisible particles depend critically on the accuracy of these vertex measurements. Additionally, the calculation inherits uncertainties from the  $B^0$  mass estimation, where non-physical reconstructed masses exceeding the theoretical value were observed (as mentioned in Section IV A 1)), potentially amplifying the resulting errors.

More fundamentally, our approach corrects the longitudinal momentum component of the  $B^0$  candidate using a mass-scaling constraint and reconstructs the transverse components by projecting along the reconstructed flight direction, defined by the vector from the primary vertex to the decay vertex. This procedure effectively aligns the corrected momentum direction with the measured geometric decay path. As a result, any genuine transverse missing momentum—such as that arising from escaping neutral particles—is absorbed into a directional bias, rather than being explicitly reconstructed.

Among all the reconstructed quantities, the fraction of non-physical or abnormal values is generally below 1%, with the exception of NaN entries found in the missing mass of the signal sample. Given their small proportions, we assume that these abnormal values have negligible impact on the analysis and therefore do not explicitly correct them.

For the NaN values observed in the signal missing mass, we computed the squared missing mass, resulting in negative values. Although these negative values are non-physical, they may carry useful information for machine learning models by signaling anomalous event kinematics. This approach is preferable to keeping NaNs, which would require imputation or special handling during model training and could introduce additional biases. By converting NaNs into defined numerical values, we maintain numerical stability and allow the classifier to naturally learn to treat such events differently if beneficial.

## C. Frame Boosting

### 1) Computation

To enhance the separation between signal and background, we performed a Lorentz boost of all kinematic variables into the estimated rest frame of the  $B^0$  meson. This transformation, inspired by Ref. [26] and built upon the corrected  $B^0$  kinematics discussed in Section V 1), reduces event-level momentum smearing and reveals intrinsic angular and energy patterns in the final-state

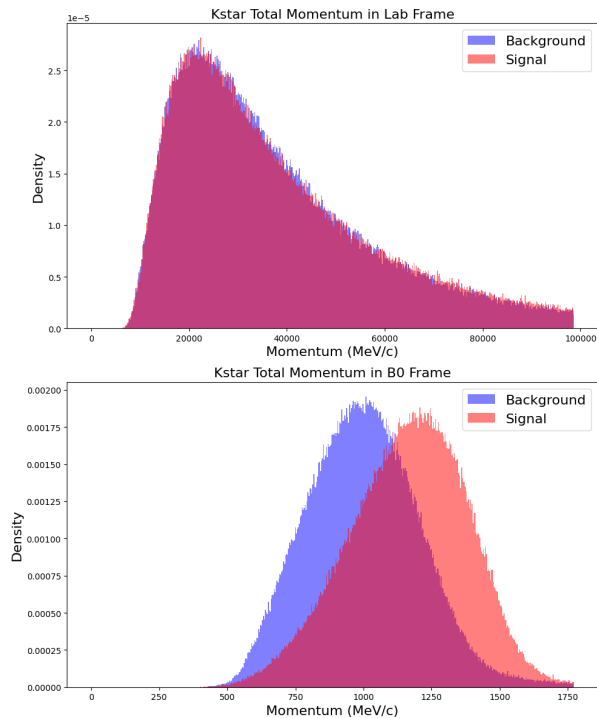


Figure 21: Momentum distribution of `kstar_P` in the lab frame (upper plot) and in the  $B^0$  rest frame (lower plot). Signal and background exhibit significant overlap in the lab frame whereas their separation becomes clearer in the  $B^0$  rest frame.

particles. Boosting to the  $B^0$  rest frame provides a more natural representation of the decay topology and enables the construction of frame-invariant observables for physics-aware feature engineering.

The Lorentz transformation for a boost along velocity vector  $\vec{v}$  is given by:

$$\Lambda_{\vec{v}}^{\mu} = \delta_{\nu}^{\mu} + (\gamma - 1) \frac{v^{\mu} v_{\nu}}{v^2} - \gamma \frac{v^{\mu} u_{\nu} + u^{\mu} v_{\nu}}{c}. \quad (33)$$

In this expression,  $\Lambda_{\vec{v}}^{\mu}$  denotes the components of the Lorentz transformation matrix, which maps four-vectors between inertial frames in relative motion. The symbol  $\delta_{\nu}^{\mu}$  is the Kronecker delta, acting as the identity matrix in Minkowski space. The quantity  $v^{\mu}$  represents the four-velocity of the boosted frame, typically written in the lab frame as  $v^{\mu} = (0, \vec{v})$ , where  $\vec{v} = (v_x, v_y, v_z)$  is the three-velocity of the particle. To isolate the time component during the transformation, we introduced the unit time-like four-vector  $u^{\mu} = (1, 0, 0, 0)$ . The Lorentz factor  $\gamma$ , which accounts for relativistic time dilation and length contraction, is given by  $\gamma = 1/\sqrt{1 - v^2/c^2}$ . Here, the three-velocity  $\vec{v}$  is derived from the particle's momentum and energy via  $\vec{v} = \vec{p}/E$ , where  $\vec{p} = (p_x, p_y, p_z)$  denotes the spatial momentum and  $E$  is the total energy.

Applying this transformation, the four-momentum  $p^{\mu}$  in the lab frame was boosted to the  $B^0$  rest frame via:

$$p^{\mu} = \Lambda_{\vec{v}}^{\mu} p^{\nu}. \quad (34)$$

Table 3 presents the KS statistics for the momentum ( $P$ ) and transverse momentum ( $P_T$ ) of selected particles, evaluated in both the lab frame and the  $B^0$  rest frame. These two variables were chosen as representative of longitudinal and transverse kinematic components, respectively.

The Lorentz transformation consistently amplifies the separation between signal and background across all kinematic features. Among them, `kstar_P` exhibits the

Table 3: KS STATISTICS IN LAB FRAME AND  $B^0$  REST FRAME

Variable	Lab Frame	$B^0$ Rest Frame	%Increase
$K^{\pm} P$	0.027	0.134	396
$K^{\pm} P_T$	0.035	0.108	209
$\pi^{\mp} P$	0.033	0.185	461
$\pi^{\mp} P_T$	0.083	0.155	87
$\mu^+ P$	0.066	0.171	159
$\mu^+ P_T$	0.113	0.158	40
$\mu^- P$	0.065	0.168	158
$\mu^- P_T$	0.114	0.155	36
$K^* P$	0.015	0.321	2040
$K^* P_T$	0.068	0.250	268
$J/\psi P$	0.078	0.236	203
$J/\psi P_T$	0.136	0.219	61

largest increase in KS statistic—rising by 2040% from the lab frame ( $p = 3 \times 10^{-37}$ ) to the  $B^0$  rest frame ( $p \approx 0$ )—indicating a substantial improvement in discriminating power. As discussed in Section IV A 1), the reconstructed  $K^*$  momentum is typically higher in signal events. Boosting to the  $B^0$  rest frame further magnifies this distinction by eliminating event-level motion, as illustrated in Fig. 21. This demonstrates how rest-frame observables enhance classification performance by emphasizing intrinsic decay kinematics. The plots for other variables are provided in Appendix D.

## 2) Discussions and Uncertainties

To validate the correctness of the Lorentz transformation, we directly tested whether invariant quantities are preserved before and after the boost. Specifically, for each visible final-state particle, we compared the invariant mass  $m^2 = E^2 - |\vec{p}|^2$  squared computed from its four-momentum in the lab frame and in the  $B^0$  rest frame.

For all particles involved—kaon, pion, and muons—we observed that the mass squared values computed before and after the boost were consistent to within numerical precision (absolute difference  $\sim 10^{-7}$  MeV<sup>2</sup>). This confirms that the Lorentz transformation has been implemented correctly and that no significant distortions are introduced during the frame change. Histograms illustrating the absolute differences in invariant mass squared before and after the Lorentz boost can be found in Appendix D.

Moreover, this test provides an event-by-event validation that the boost matrix is physically valid (i.e., does not contain unphysical parameters such as superluminal velocities). No events were found to violate Lorentz invariance, and no negative mass squared values appeared post-boost.

Although the boost relies on the reconstructed  $B^0$  four-momentum and thus inherits all associated uncertainties discussed in Section V 1), these do not appear to compromise the numerical stability or physical consistency of the Lorentz transformation. The observed invariance of mass-squared quantities across frames suggests that the transformation was implemented correctly and robust against moderate reconstruction errors.

## D. Geometric Separation

### 1) Computation

As discussed in Section IV A. 1), signal decays are expected to exhibit larger geometric separation between the kaon and pion, as well as between the two muons, due to increased kinematic randomness introduced by the lighter  $\tau$  leptons and neutrinos. In this study, we focus on the differences in angular variables between signal and background, including azimuthal angle, pseudorapidity, angular distance  $\Delta R$ , and pairwise opening angles between decay products.

The azimuthal angle  $\phi$  is defined as the angle between a particle's momentum vector and the x-axis in the transverse (x-y) plane. In LHCb experiments, where the beam direction is aligned along the z-axis, the transverse plane is orthogonal to the beam line. Accordingly, the azimuthal angle can be computed using:

$$\phi = \tan^{-1} \left( \frac{p_y}{p_x} \right) \quad (35)$$

Here,  $p_x$  and  $p_y$  represent the components of the particle's momentum in the transverse plane.

To quantify the angular separation between two particles in the transverse plane, the difference in their azimuthal angles, denoted as  $\Delta\phi$ , can be computed as:

$$\Delta\phi = \begin{cases} |\phi_1 - \phi_2|, & \text{if } |\phi_1 - \phi_2| \leq \pi \\ 2\pi - |\phi_1 - \phi_2|, & \text{if } |\phi_1 - \phi_2| > \pi \end{cases} \quad (36)$$

This definition ensures that the azimuthal angle difference  $\Delta\phi$  always lies within the range  $[0, \pi]$ , accounting for the periodicity of the angular coordinate.

Pseudorapidity ( $\eta$ ) is a spatial coordinate that describes the angle of a particle relative to the beam axis (z-axis), defined as:

$$\eta = -\ln \left( \tan \frac{\theta}{2} \right), \quad (37)$$

where  $\theta$  is the polar angle between the particle's momentum vector and the beam axis.  $\eta$  is invariant under Lorentz boosts along the beam axis, making it particularly useful in collider experiments where particles are highly boosted in the longitudinal direction [27].

Similar to the azimuthal angle difference, the pseudorapidity difference between two particles is calculated using an absolute difference.

By combining longitudinal and transverse angular separations into a rotationally invariant quantity, the angular distance  $\Delta R$  provides a robust measure of spatial separation between two particles in the detector. It is defined as:

$$\Delta R = \sqrt{(\Delta\eta)^2 + (\Delta\phi)^2} \quad (38)$$

A small value of  $\Delta R$  indicates that the two particles are close in angular space, suggesting that they are more likely to be collimated and share similar directions.

Similarly, the opening angle  $\theta$  between two momentum vectors  $\vec{p}_1$  and  $\vec{p}_2$  is defined as:

$$\cos \theta = \frac{\vec{p}_1 \cdot \vec{p}_2}{|\vec{p}_1| |\vec{p}_2|}, \quad (39)$$

where the numerator represents the dot product of the two vectors, and the denominator is the product of their magnitudes. The method of handling periodicity in angle differences follows the same logic as in Eq. 36.

To evaluate the separation power of geometric features,

the KS test was applied to each pairwise angular variable (Table 4). The kaon-pion separation is larger in signal events than in background. This arises from the underlying decay topologies: while the kaon and pion originate directly from the  $B^0$  in both cases, the heavier  $D^\pm$  mesons in the background ( $B^0 \rightarrow K^\pm \pi^\mp D^+ D^-$ ) carry more longitudinal momentum and impose stronger directional constraints, yielding narrower separations.

By similar reasoning, one might expect muon-muon separation to also differ between signal and background due to the heavier mass of the  $K^0$  (background) relative to the neutrinos (signal). However, no significant difference was observed in angular distances. This is primarily because the two muons originate from separate  $D^\pm$  or  $\tau^\pm$  decays, and both channels involve neutrinos, which introduce additional angular smearing. As a result, only the kaon-pion geometric separation features were retained. Plots of these separation variables are provided in Appendix E.

Table 4: KS STATISTICS BETWEEN SIGNAL AND BACKGROUND

Variable	$K^\pm, \pi^\mp$	$\mu^+, \mu^-$
$\Delta\phi$	0.0894	0.0129
$\Delta\eta$	0.0616	0.0186
$\Delta R$	0.1222	0.0201
$\theta$	0.1139	0.0428

### 2) Discussions and Uncertainties

The three-momentum components ( $p_x, p_y, p_z$ ) of the reconstructed final-state particles are subject to finite detector resolution and tracking uncertainties. These uncertainties propagate into angular variables such as the azimuthal angle  $\phi$ , pseudorapidity  $\eta$ , opening angle, and pairwise angular distances, potentially smearing the distributions and reducing their separation power. Despite these effects, angular features were retained since some of the angular observables exhibit inherent robustness: the pseudorapidity  $\eta$  is invariant under Lorentz boosts along the beam axis, and the angular distance  $\Delta R$  is rotationally invariant in the transverse plane. These symmetries make them less sensitive to detector smearing or imperfect kinematic reconstruction, thereby supporting their continued use despite potential resolution-induced fluctuations.

## VI. RESULTS

### A. Model Performance

After feature engineering, 45 new features were created and added to the original models of both BDT and FCNN. Figure 22 and Figure 23 compare the predicted probability distributions for the original and extended BDT models, respectively (the corresponding results for FCNN are provided in Appendix F). The dashed lines indicate the optimal classification thresholds determined via F1 score maximization, as described in Section IV B 1). Events with predicted probabilities to the left of the threshold are classified as background, and those to the right as signal.

Compared to the original model, the probability distribution after feature engineering exhibits significantly sharper peaks near 0 and 1, along with a substantial reduction in the density of intermediate probabilities. This suggests that the addition of engineered features improves the model’s ability to separate signal from background, resulting in more confident predictions and enhanced performance in precision, recall, and overall classification accuracy.

This improvement is quantitatively reflected by more than a 3% increase in AUC-ROC scores for both models: from 0.841 to 0.877 for FCNN, and from 0.860 to 0.912 for BDT. For reference, the corresponding results for the FCNN model and the ROC curves for both models are provided in Appendix F. The performance metrics for both models are summarized in Table 5.

Table 5: COMPARISON OF CLASSIFICATION METRICS FOR FCNN AND BDT, WITH RELATIVE IMPROVEMENTS

Metric	Model	Value	% Increase
Accuracy	FCNN	$0.777 \pm 0.001$	3.37
	BDT	$0.822 \pm 0.002$	5.38
Precision	FCNN	$0.756 \pm 0.004$	5.63
	BDT	$0.799 \pm 0.004$	7.97
Recall	FCNN	$0.840 \pm 0.002$	0.84
	BDT	$0.860 \pm 0.005$	2.38
F1-score	FCNN	$0.799 \pm 0.001$	3.86
	BDT	$0.833 \pm 0.001$	5.84
ROC AUC	FCNN	$0.877 \pm 0.000$	4.28
	BDT	$0.912 \pm 0.000$	6.04

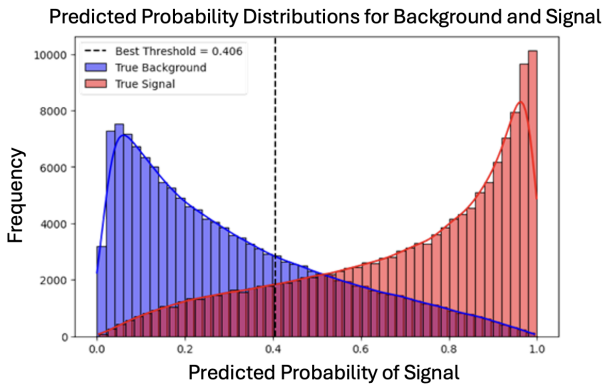


Figure 22: Histogram of predicted probabilities on the raw dataset, showing true background and true signal distributions. An optimal classification threshold at 0.406 is marked. The overlap between background and signal highlights the trade-off between predictive performance and real-world ambiguity.

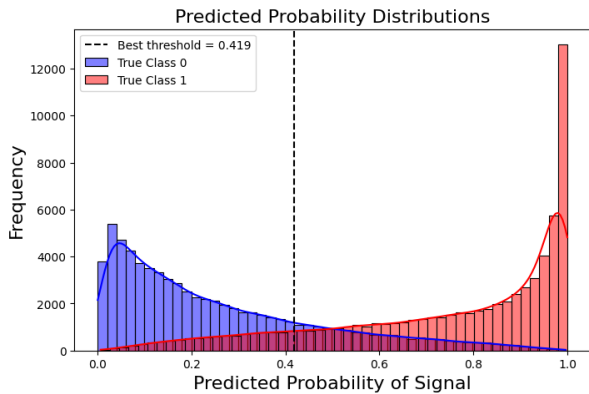


Figure 23: Histogram of predicted probabilities after feature engineering, showing overlapping background and signal, with a threshold at 0.419. The overlapped region is smaller than that in the raw dataset.

Across all metrics, the standard deviations from cross-validation are small, indicating that the models are stable and yield consistent results across different data splits. Building upon this stability, we observe an overall increase in all evaluation scores after feature engineering. These improvements are consistent and exceed the statistical uncertainties introduced by cross-validation, confirming that the observed enhancements are both robust and statistically significant. Notably, the

increase in F1-score—3.86% for FCNN and 5.84% for BDT—demonstrates a better-balanced trade-off between signal recovery (recall) and prediction precision, highlighting the improved reliability of both classifiers.

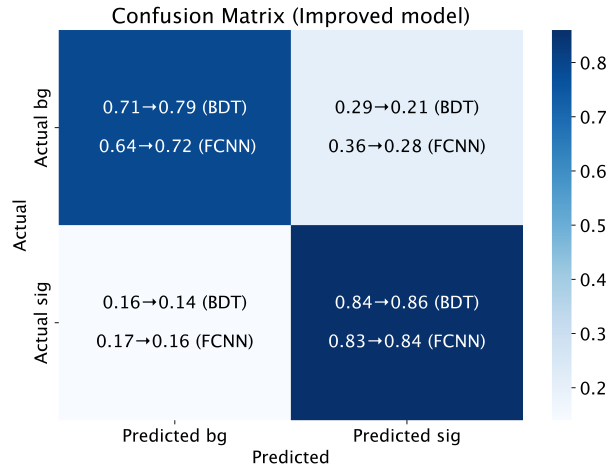


Figure 24: Normalized (along each row) confusion matrix for the BDT and FCNN at their respective optimal F1-score thresholds before and after model improvement.

As shown in Fig. 24, feature engineering leads to a clear reduction in background misclassification. The proportion of background events incorrectly predicted as signal drops by 8% for both models, improving the upper-right quadrant of the confusion matrix. This results in a lower contamination rate in the predicted signal class and hence a higher precision. For instance, in the BDT model, the precision improves from 74.0% to 79.9% after feature engineering, indicating that the predicted signal events are now purer and more reliable.

In addition to improved background identification, both models also exhibit marginal gains in correctly identifying signal events. The true positive rate increases from 83% to 84% in FCNN, and from 84% to 86% in BDT. While these gains are relatively modest, they are built on already high recall baselines and are achieved alongside significant improvements in background suppression. Together, these results highlight the effectiveness of feature engineering in enhancing both the precision and sensitivity of the classifiers.

## B. Feature Importance

We performed feature permutation importance analysis with new features. Top 5 features for BDT and FCNN models are presented in Fig.25. Among these features, three are shared by both the BDT and FCNN models. Furthermore, within the top 20 features, 80% overlap is observed between the two models, indicating the most discriminative features are not only statistically relevant but also robust across different modelling approaches. It reinforces the reliability of feature importance rankings and supports the physical interpretability of the selected variables. In addition, for both the BDT and FCNN models, 6 out of the top 10 features are newly engineered, highlighting the substantial contribution of the new features to model performance. This proves the success of our feature engineering.

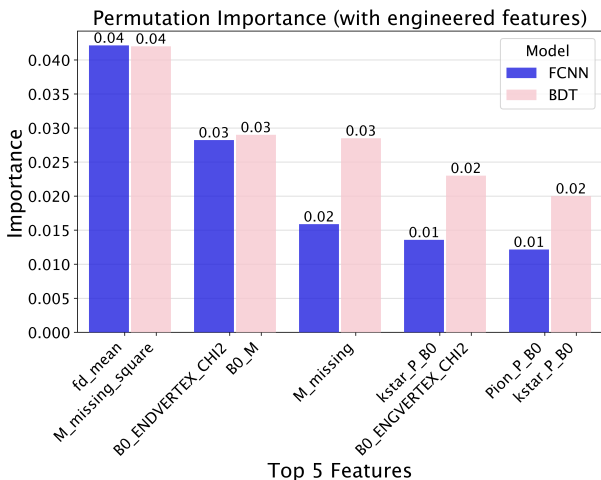


Figure 25: Top 5 features ranked by permutation importance for FCNN and BDT models after including engineered features.

The engineered features are composite in nature, with combined information from multiple kinematic variables. This aligns with the pattern observed in Section IV A, where composite features consistently outperform raw measurements of individual particles, as they better capture correlations and higher-level decay structures. Specifically, 100% for the BDT and 95% for the FCNN of the top 20 features are composite features.

Furthermore, after removing the engineered features, the ranking of the original variables shows minimal variation, with no feature exhibiting a shift of more than five positions. For instance, both B0\_M and B0\_ENDVERTEX\_CHI2 were originally the top two features and remain the top two among the original features, as well as within the top five overall. This indicates that the originally informative features continue to play a significant role, and their importance is not suppressed or replaced by the inclusion of new features. The stability of feature importance rankings suggests that the added features provide complementary rather than redundant information.

## C. Evaluations

Although feature engineering substantially improved background identification—as seen in the upper-left quadrant of the confusion matrix—it remains less effective than signal retention in the lower-right quadrant. This

asymmetry arises partly from the intrinsic similarity between some background and signal events, and partly from the F1-based optimization, which may favour high recall for the signal class when signal-like features are more distinctive. As a result, the model is more confident in identifying true signals than rejecting all backgrounds.

In addition to classification limitations, the analysis is also affected by several sources of uncertainty. First, the original dataset contains inherent uncertainties from track reconstruction and particle identification, which propagate into the momentum and energy measurements of final-state particles. These uncertainties influence both raw kinematic features and all derived observables constructed through feature engineering.

Engineered features, in particular, not only inherit and potentially amplify the uncertainties present in the original variables, but also introduce new sources of error due to modeling assumptions and numerical approximations. For instance, the computation of the  $B^0$  missing mass relies on mass-scaling approximations of the visible momentum; frame boosting requires a Lorentz transformation based on reconstructed directions and energies, which may accumulate floating-point rounding errors and angular resolution mismatches. These effects can result in reduced separation power in regions of phase space.

However, as discussed in previous sections, we have carefully examined these engineered features and addressed the most significant sources of instability through both analytical checks (e.g., frame-invariant tests) and numerical validations (e.g., mass consistency histograms). Despite these remaining uncertainties, the improved AUC and precision scores suggest that the engineered features remain robust against moderate levels of noise and modeling error. Nevertheless, future work should aim to further quantify and mitigate such uncertainties, particularly in the context of physics-sensitive downstream analyses where small biases can propagate into systematic deviations.

## VII. CONCLUSION AND OUTLOOK

This project explored the use of supervised machine learning to distinguish the rare decay  $B^0 \rightarrow K^{*0} \tau^+ \tau^-$  from the dominant background  $B^0 \rightarrow K^{*0} D^+ D^-$ , which shares the same visible final state. Using simulated LHCb data, we trained and evaluated two representative models—a fully connected neural network (FCNN) and a boosted decision tree (BDT).

Starting from raw inputs, we performed feature selection and parameter tuning, then constructed high-level physical features based on decay topology, vertex displacement, and frame-dependent kinematics. These engineered features significantly improved model performance.

Evaluation showed that the model is more effective at retaining true signal events than rejecting background. In realistic applications, predicted signal candidates are typically retained for further analysis. Under the current threshold, the model achieves a precision of about 0.80, implying 20% background contamination—potentially problematic for downstream observables. This can be mitigated by increasing the threshold to improve purity, at the cost of reduced recall.

Furthermore, the two structurally distinct models we trained—a FCNN and a BDT should achieve similar performance ideally, as the underlying physics is model-independent and should be learnable regardless of architecture. In our current results, however, the BDT achieves stronger performance than the FCNN across most evaluation metrics. This difference may indicate that the FCNN, under its current configuration, has not yet fully learned to extract or utilize the most discriminative features in the data. Possible reasons include insufficient model capacity, suboptimal hyperparameter choices, or the inherent advantage of BDTs in modeling tabular, structured features [28]. While the observed gap does not invalidate the use of FCNNs, it highlights the importance of further exploration into neural architectures or training strategies that are better suited to this problem.

Overall, this work demonstrates the feasibility of applying interpretable machine learning to rare decay classification in high-energy physics. The methods developed in this project can be applied to real LHCb analyses, particularly in early stages such as event preselection or filtering. In addition, the approach can be extended to other decay channels or adapted to multi-class classification problems, making it broadly useful for future studies in flavor physics.

# APPENDIX

## A. Additional Feynman Diagrams

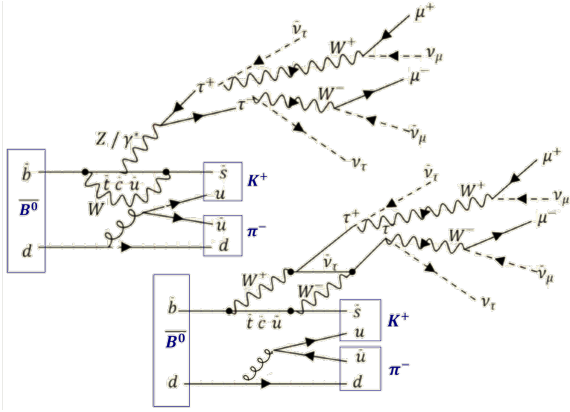


Figure 26: Feynman diagram of the signal process  $\bar{B}^0 \rightarrow K^+ \pi^- \mu^+ \mu^-$  after  $B^0$ - $\bar{B}^0$  mixing.

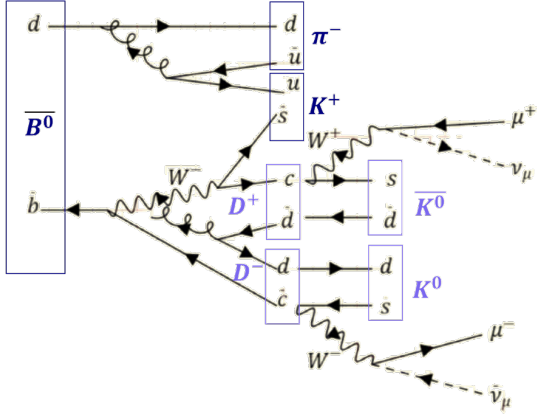


Figure 27: Feynman diagram of the background process  $\bar{B}^0 \rightarrow K^+ \pi^- \mu^+ \mu^-$  after  $B^0$ - $\bar{B}^0$  mixing.

## B. Additional BDT Hyperparameter Search

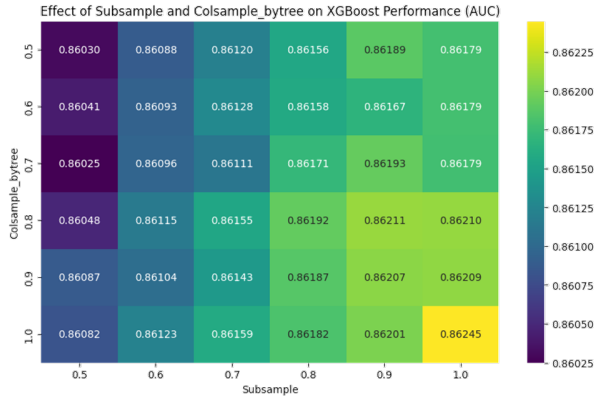


Figure 28: Grid search results showing the impact of `subsample` and `colsample_bytree` on XGBoost performance (AUC). Each cell represents the AUC score obtained with the corresponding parameter combination. The best performance is achieved with `subsample = 1.0` and `colsample_bytree = 1.0`.

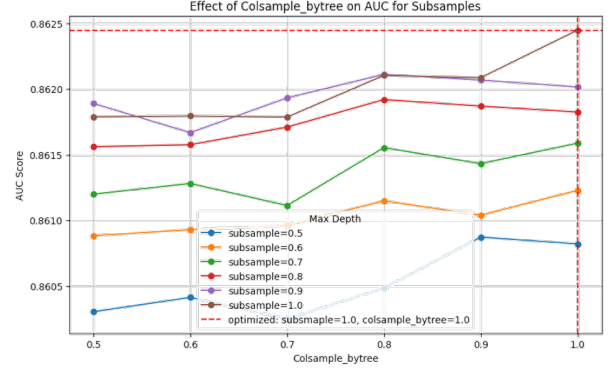


Figure 29: Effect of `colsample_bytree` on AUC scores across different `subsample` values.

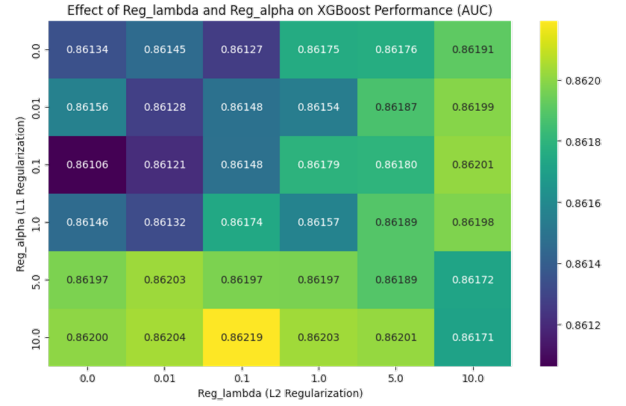


Figure 30: Grid search results showing the effect of `reg_lambda` (L2 regularization) and `reg_alpha` (L1 regularization) on XGBoost performance. AUC scores are shown for each parameter combination. The highest score is achieved at `reg_lambda = 0.1` and `reg_alpha = 10.0`.

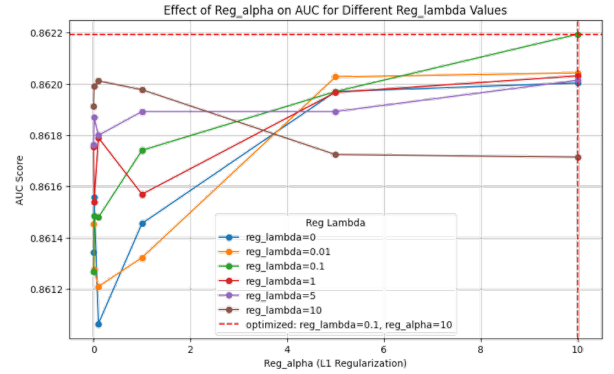


Figure 31: Line plot showing the effect of `reg_alpha` (L1 regularization) on AUC scores under different values of `reg_lambda` (L2 regularization). Each curve corresponds to a fixed `reg_lambda` value.

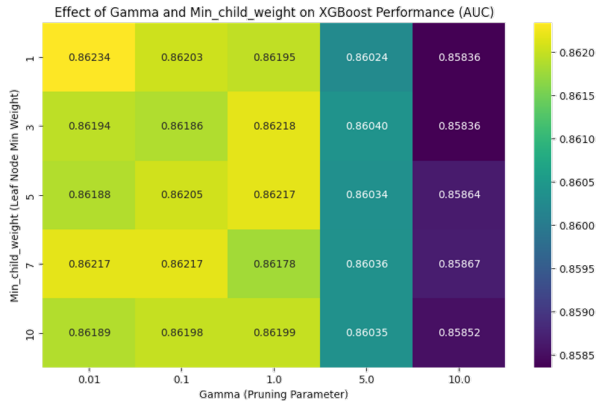


Figure 32: Grid search results showing the effect of  $\gamma$  and  $\text{min\_child\_weight}$  on XGBoost performance (AUC). The best result is achieved with  $\gamma = 0.01$  and  $\text{min\_child\_weight} = 1.0$ .

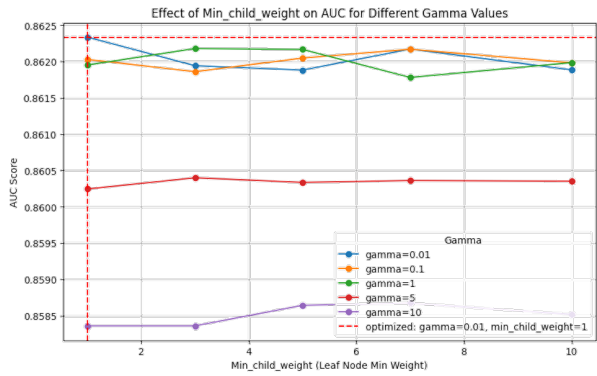


Figure 33: Line plot showing the effect of  $\text{min\_child\_weight}$  on AUC scores for different values of  $\gamma$ . Each line corresponds to a fixed  $\gamma$  value. Excessively large values of either parameter tend to reduce model flexibility and lead to underfitting.

### C. Additional Plots for Flying Distance and Missing Mass Square

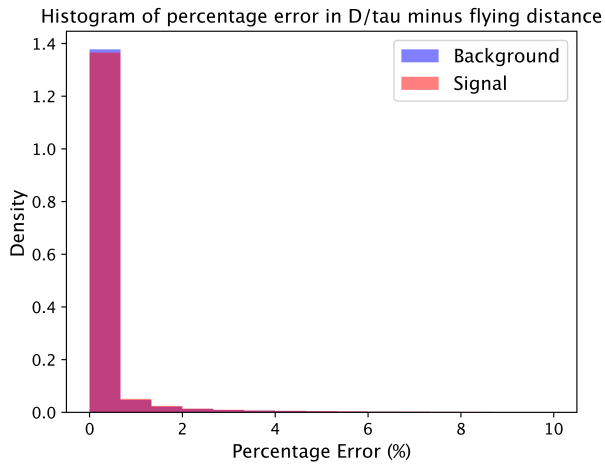


Figure 34: Distribution of the percentage error in flying distance for  $D^-/\tau^-$ , showing small errors peaking around 0. The ratio (sig) of errors exceeding 5% is 4.22%, and for background (bg) is 3.81%.

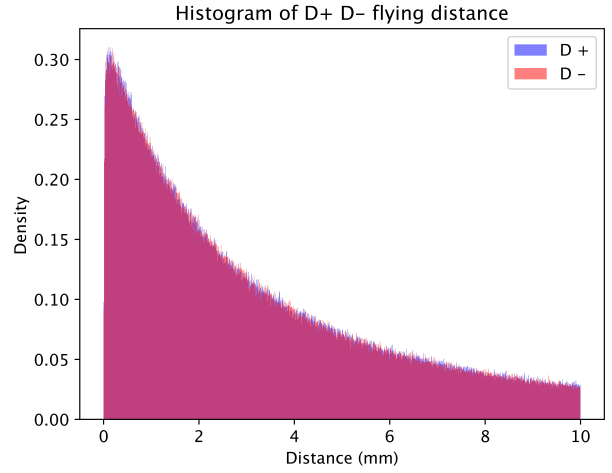


Figure 35: Distribution of the flying distance of intermediate particles  $D^-$  and  $D^+$  in background events.

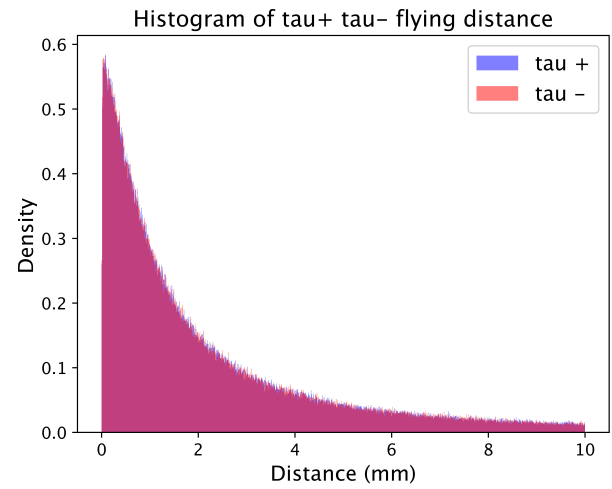


Figure 36: Distribution of the flying distance of intermediate particles  $\tau^-$  and  $\tau^+$  in signal events.

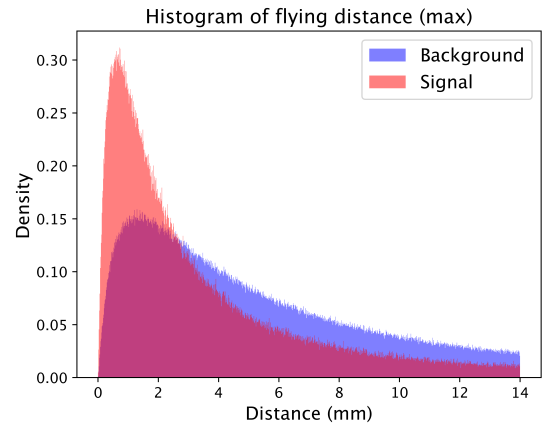


Figure 37: Distribution of the combined maximum flying distance, where the maximum value in each intermediate pair is chosen. The background intermediate particle  $D$  is compared with signal intermediate particle  $\tau$ .

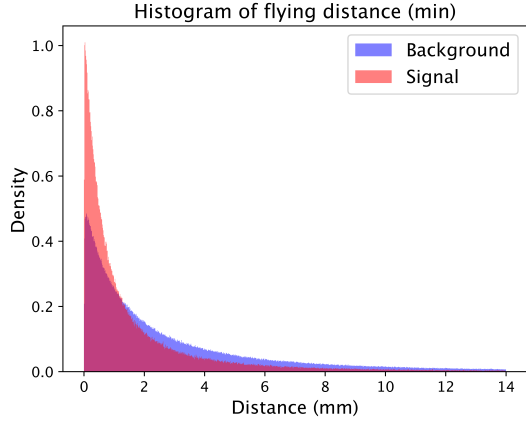


Figure 38: Distribution of the combined minimum flying distance, where the maximum value in each intermediate pair is chosen. The background intermediate particle  $D$  is compared with signal intermediate particle  $\tau$ .

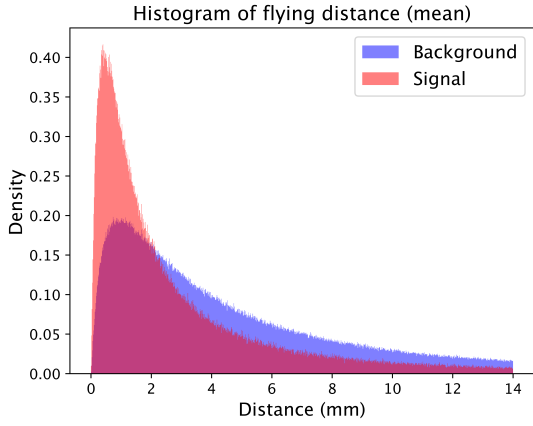


Figure 39: Distribution of the combined minimum flying distance, where the mean value in each intermediate pair is chosen. The background intermediate particle  $D$  is compared with signal intermediate particle  $\tau$ .

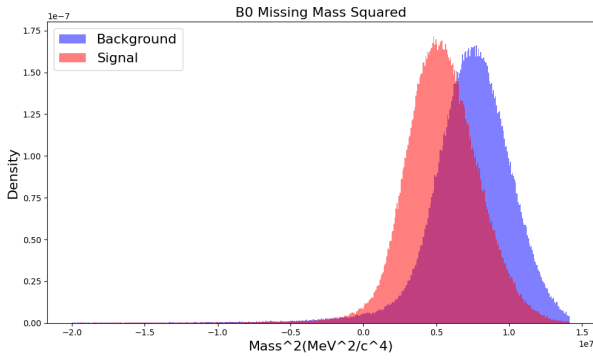


Figure 40: Distribution of the squared missing mass  $M_{\text{miss}}^2$  of  $B^0$ . Negative values are observed in the signal sample.

#### D. Additional Plots for Frame Boosting

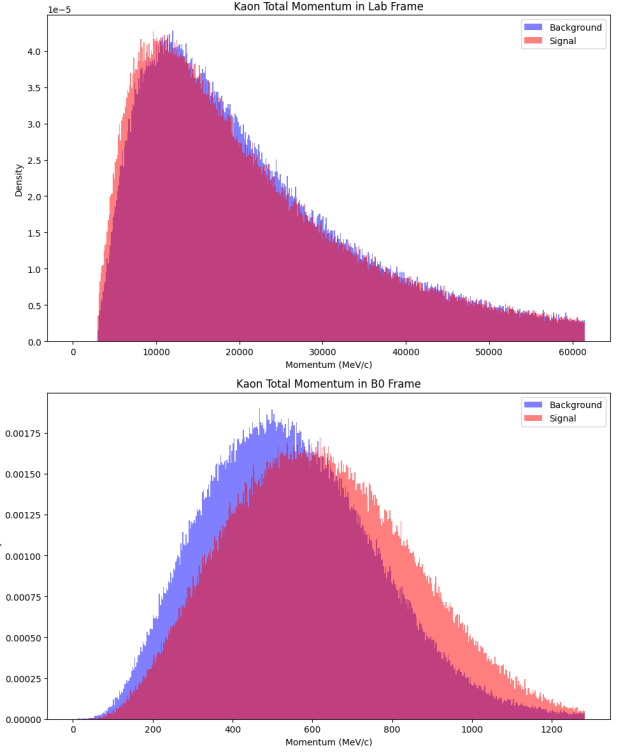


Figure 41: The upper plot shows the  $K^\pm$  total momentum distribution in the Lab Frame and the lower plot shows the distribution in the  $B^0$  rest frame. The KS statistics for the Lab Frame and  $B^0$  Rest Frame are 0.027 and 0.134, respectively, with a 396% increase.

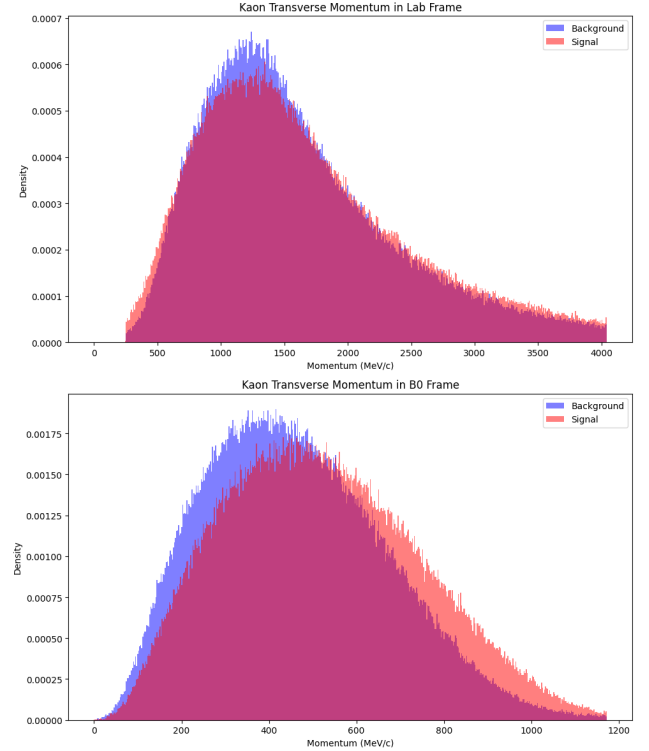


Figure 42: The upper plot shows the  $K^\pm$  transverse momentum distribution in the Lab Frame and the lower plot shows the distribution in the  $B^0$  rest frame. The KS statistics for the Lab Frame and  $B^0$  Rest Frame are 0.035 and 0.108, respectively, with a 209% increase.

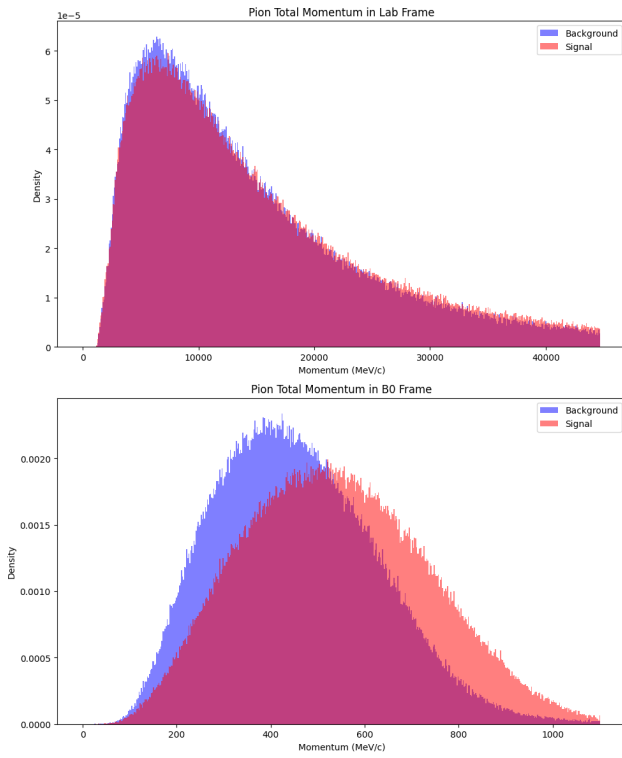


Figure 43: The upper plot shows the  $\pi^\pm$  total momentum distribution in the Lab Frame and the lower plot shows the distribution in the  $B^0$  rest frame. The KS statistics for the Lab Frame and  $B^0$  Rest Frame are 0.033 and 0.185, respectively, with a 461% increase.

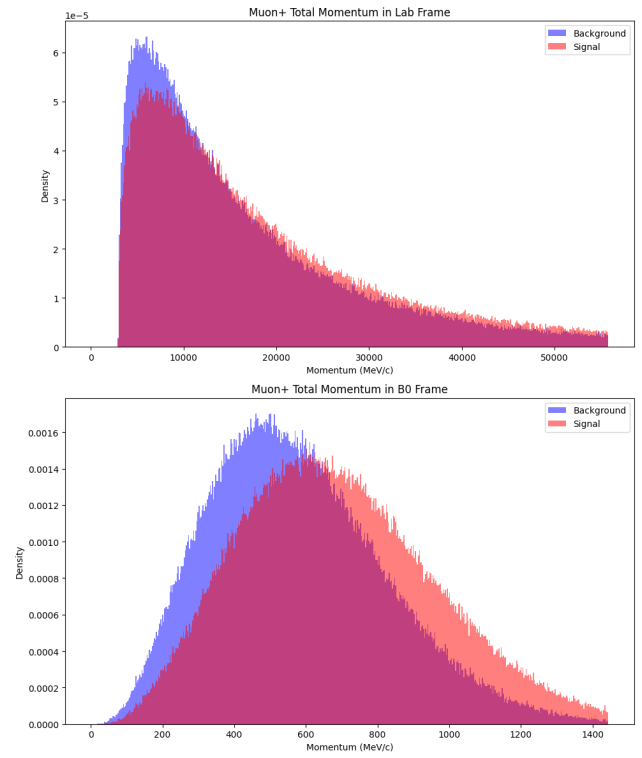


Figure 45: The upper plot shows the  $\mu^+$  total momentum distribution in the Lab Frame and the lower plot shows the distribution in the  $B^0$  rest frame. The KS statistics for the Lab Frame and  $B^0$  Rest Frame are 0.066 and 0.171, respectively, with a 159% increase.

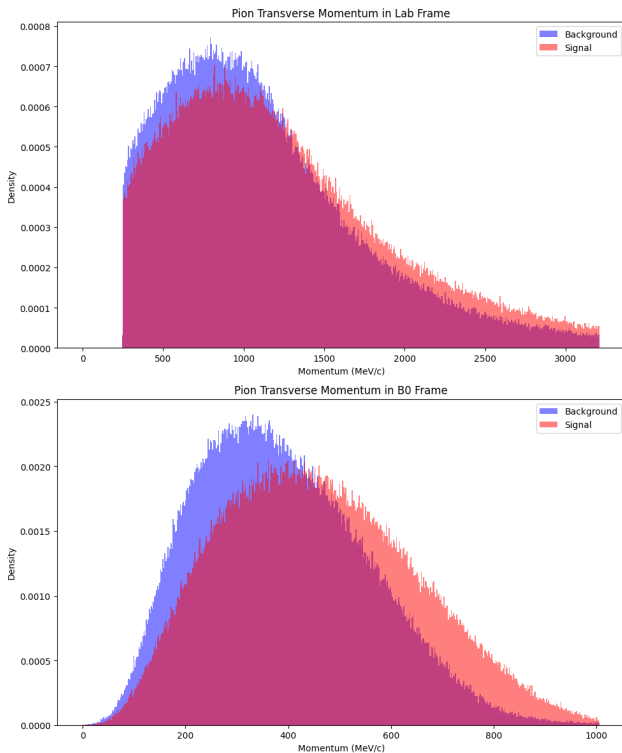


Figure 44: The upper plot shows the  $\pi^\pm$  transverse momentum distribution in the Lab Frame and the lower plot shows the distribution in the  $B^0$  rest frame. The KS statistics for the Lab Frame and  $B^0$  Rest Frame are 0.083 and 0.155, respectively, with a 87% increase.

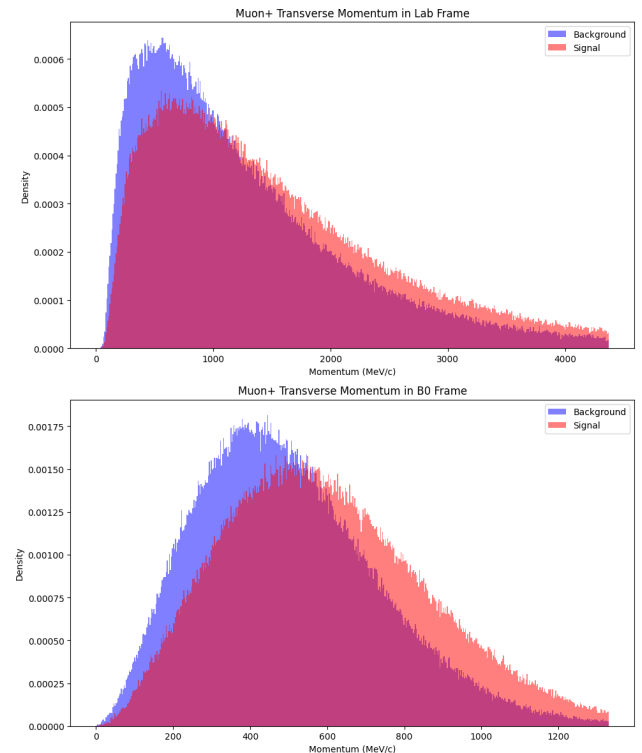


Figure 46: The upper plot shows the  $\mu^+$  transverse momentum distribution in the Lab Frame and the lower plot shows the distribution in the  $B^0$  rest frame. The KS statistics for the Lab Frame and  $B^0$  Rest Frame are 0.113 and 0.158, respectively, with a 40% increase.

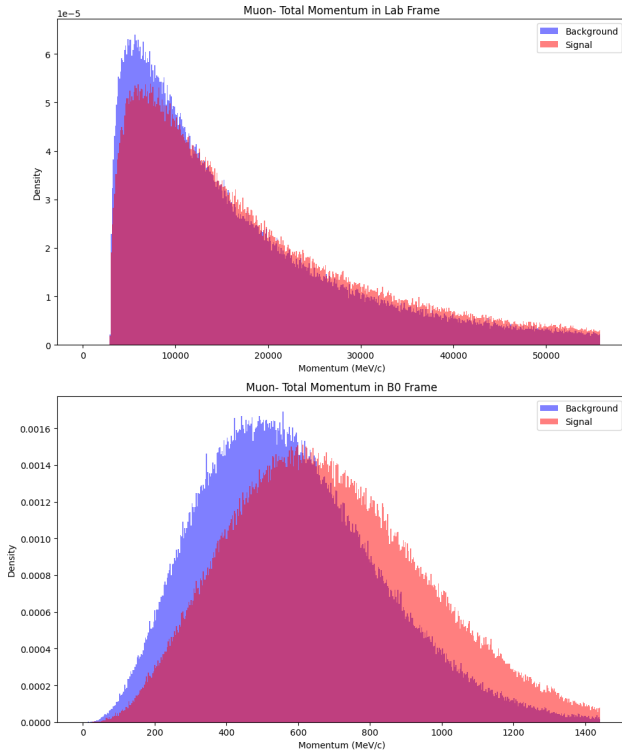


Figure 47: The upper plot shows the  $\mu^-$  total momentum distribution in the Lab Frame and the lower plot shows the distribution in the  $B^0$  rest frame. The KS statistics for the Lab Frame and  $B^0$  Rest Frame are 0.065 and 0.168, respectively, with a 159% increase.

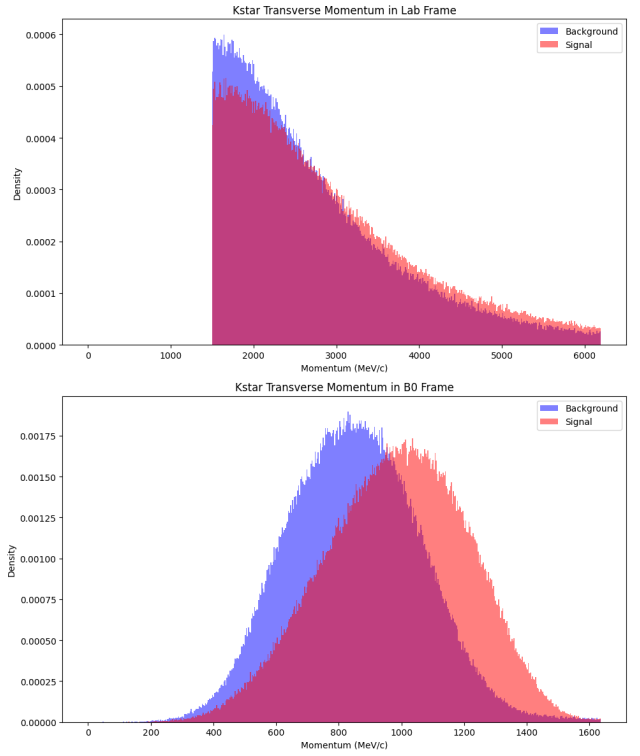


Figure 49: The upper plot shows the  $K^*$  transverse momentum distribution in the Lab Frame and the lower plot shows the distribution in the  $B^0$  rest frame. The KS statistics for the Lab Frame and  $B^0$  Rest Frame are 0.068 and 0.250, respectively, with a 268% increase.

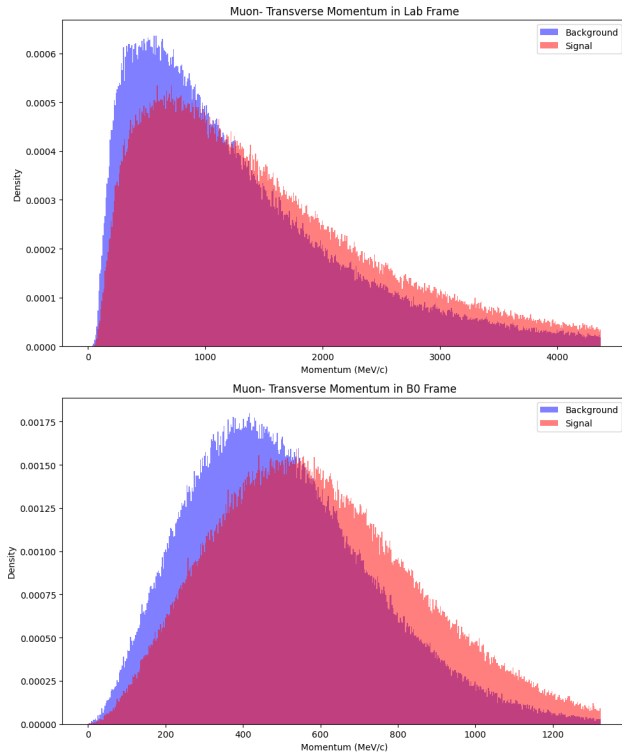


Figure 48: The upper plot shows the  $\mu^-$  transverse momentum distribution in the Lab Frame and the lower plot shows the distribution in the  $B^0$  rest frame. The KS statistics for the Lab Frame and  $B^0$  Rest Frame are 0.114 and 0.155, respectively, with a 36% increase.

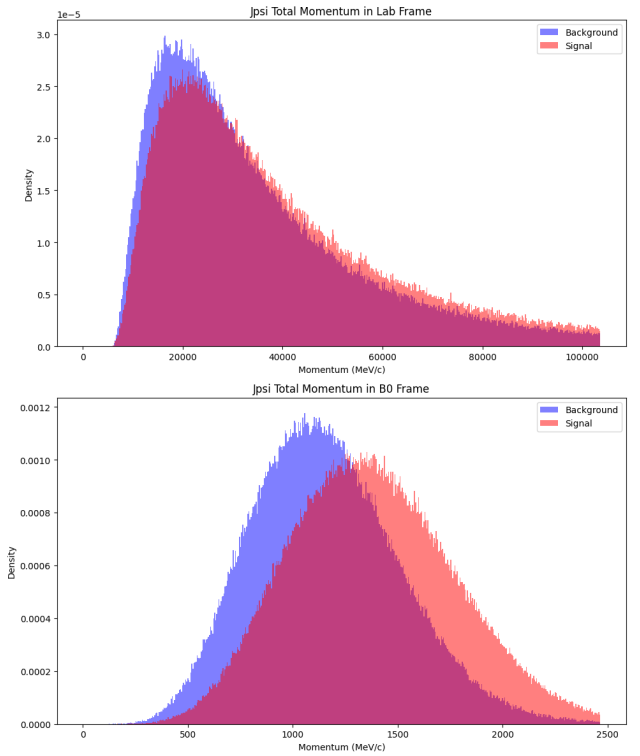


Figure 50: The upper plot shows the  $J/\psi$  total momentum distribution in the Lab Frame and the lower plot shows the distribution in the  $B^0$  rest frame. The KS statistics for the Lab Frame and  $B^0$  Rest Frame are 0.078 and 0.236, respectively, with a 203% increase.

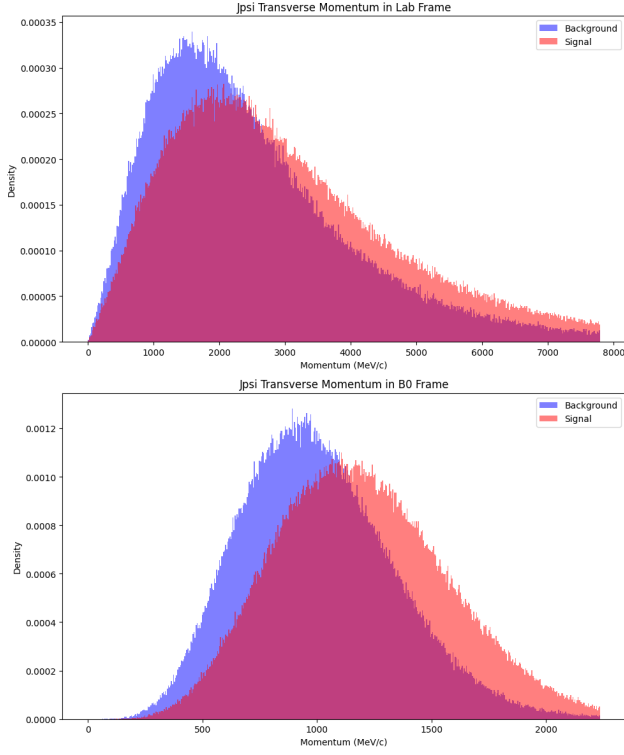


Figure 51: The upper plot shows the  $J/\psi$  transverse momentum distribution in the Lab Frame and the lower plot shows the distribution in the  $B^0$  rest frame. The KS statistics for the Lab Frame and  $B^0$  Rest Frame are 0.136 and 0.219, respectively, with a 61% increase.

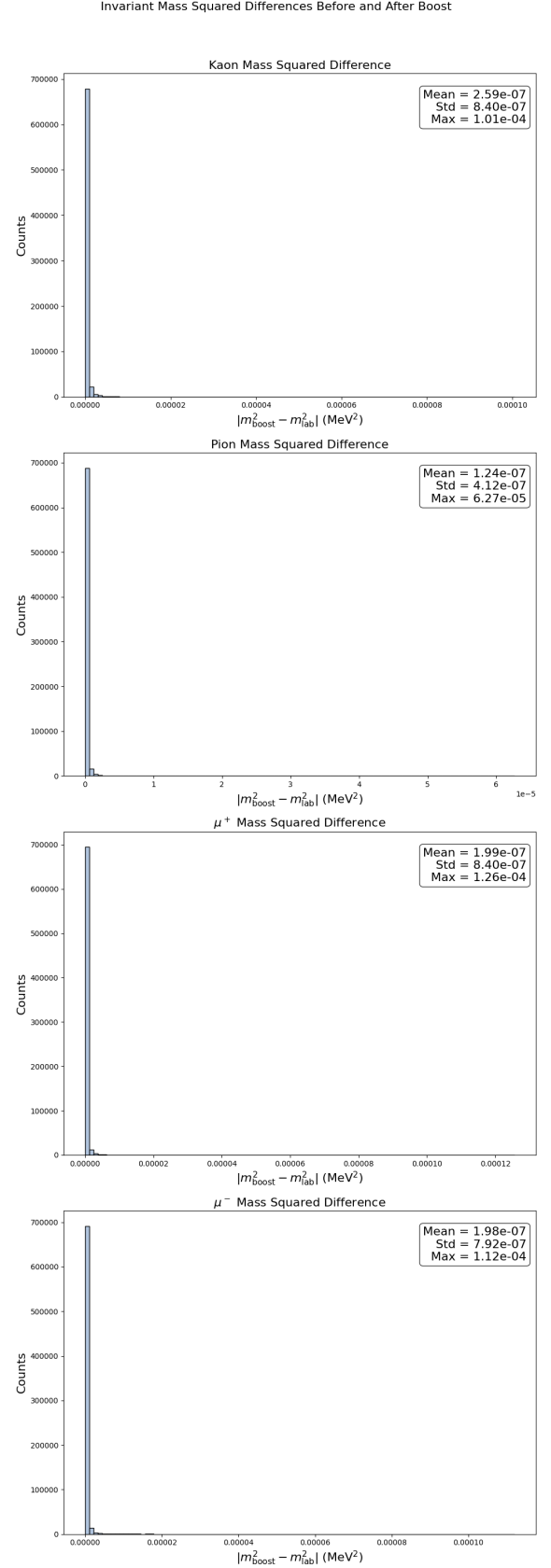


Figure 52: Invariant mass squared difference  $|m_{\text{boost}}^2 - m_{\text{lab}}^2|$  for the kaon, pion, and muons. Each panel shows the distribution of absolute mass squared differences (in  $\text{MeV}^2$ ) before and after the Lorentz boost into the  $B^0$  rest frame. The annotated values in each subpanel indicate the mean, standard deviation, and maximum of the difference. All particles exhibit minimal variation, with mean differences  $\sim 10^{-7} \text{ MeV}^2$  and max differences  $\sim 10^{-4} \text{ MeV}^2$ , demonstrating the numerical stability and Lorentz invariance of the applied transformation.

### E. Additional Plots for Geometric Separation

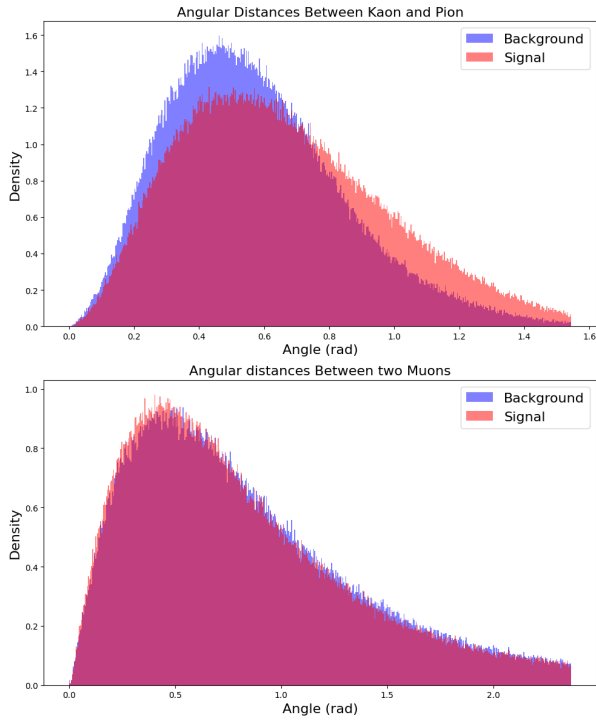


Figure 53: Top: Distribution of angular distance  $\Delta R$  between kaon and pion. Signal and background show distinct separation patterns with a KS statistic of 0.1222. Bottom: Distribution of angular distance  $\Delta R$  between muons. Signal and background exhibit overlapping distributions with a KS statistic of 0.0201, indicating weaker separation power.

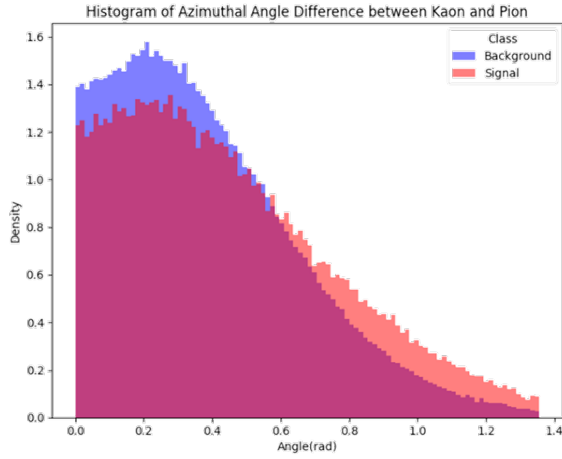


Figure 54: Distribution of the azimuthal angle difference  $\Delta\phi$  between the kaon and pion. Signal and background exhibit distinct separation patterns. KS statistic: 0.0894.

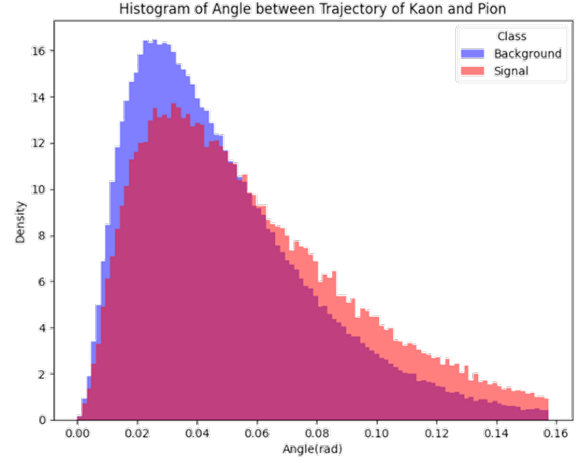


Figure 55: Distribution of the trajectory angle  $\theta$  between the kaon and pion. Signal and background separation is visible. KS statistic: 0.1139.

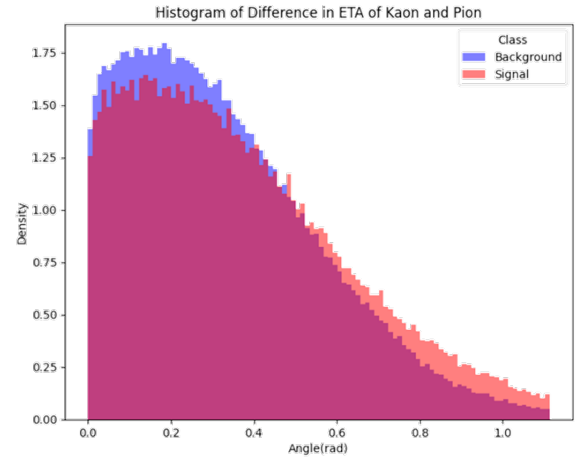


Figure 56: Distribution of the pseudorapidity difference  $\Delta\eta$  between the kaon and pion. Weak separation observed. KS statistic: 0.0616.

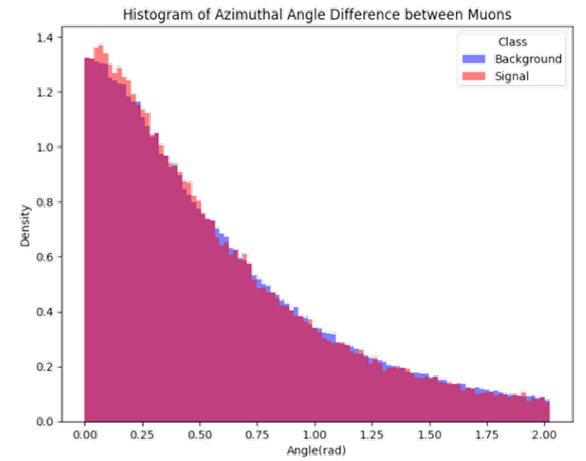


Figure 57: Azimuthal angle difference  $\Delta\phi$  between  $\mu^+$  and  $\mu^-$ . Minimal separation observed. KS statistic: 0.0129.

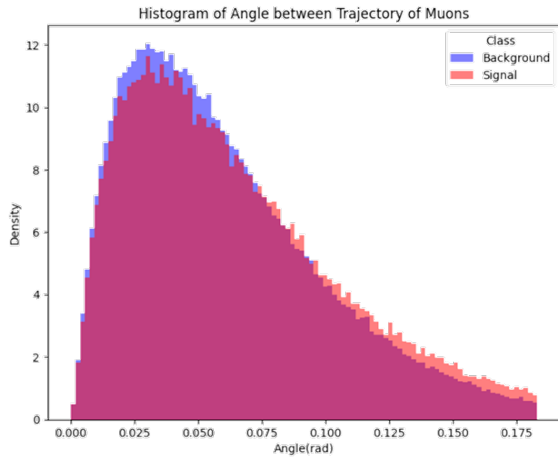


Figure 58: Trajectory angle  $\theta$  between  $\mu^+$  and  $\mu^-$ . Separation is small and likely not useful. KS statistic: 0.0428.

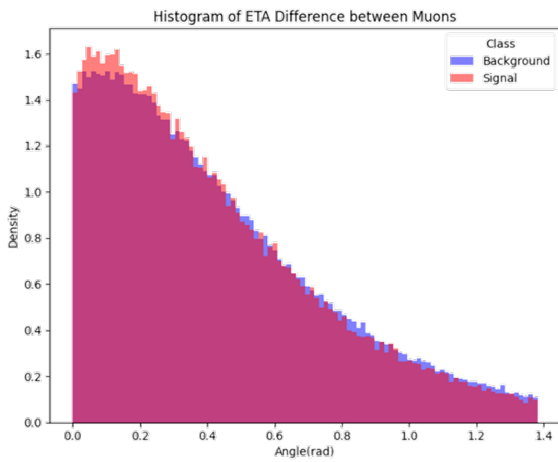


Figure 59: Pseudorapidity difference  $\Delta\eta$  between  $\mu^+$  and  $\mu^-$ . Very limited separation. KS statistic: 0.0186.

### F. Additional Model Performance Plots

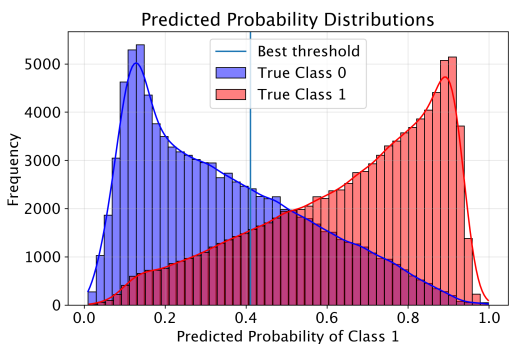


Figure 60: Probability distribution for the prediction for class 1 for the model without feature engineering.

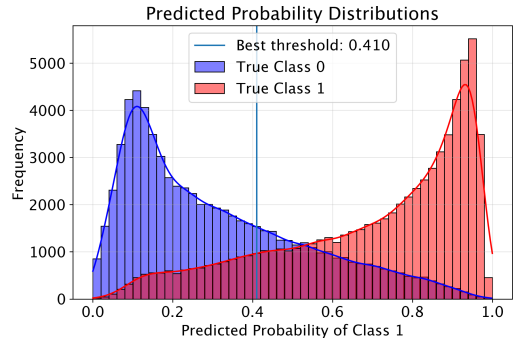


Figure 61: Probability distribution for the prediction for class 1 for the model with feature engineering.

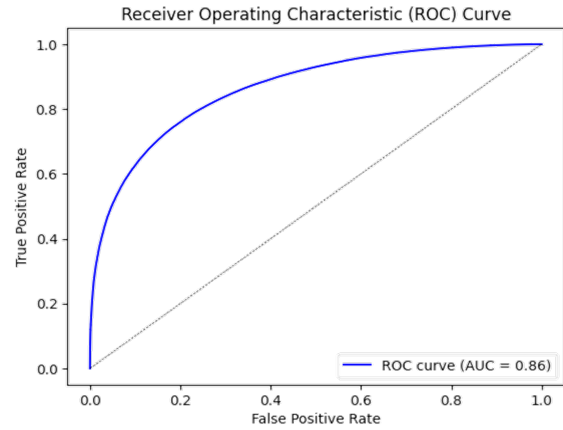


Figure 62: Receiver Operating Characteristic (ROC) curve for the BDT model before feature engineering. The classifier achieves an area under the curve (AUC) of 0.860.

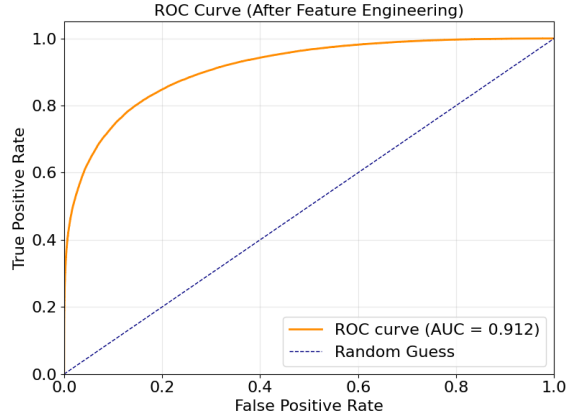


Figure 63: Receiver Operating Characteristic (ROC) curve for the BDT model after feature engineering. The classifier achieves an area under the curve (AUC) of 0.912, indicating strong separation between signal and background. The diagonal line represents the performance of a random classifier.

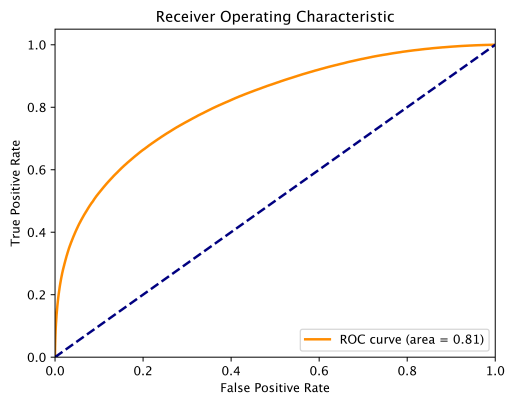


Figure 64: Receiver Operating Characteristic (ROC) curve for the FCNN model before feature engineering. The classifier achieves an area under the curve (AUC) of 0.81, indicating strong separation between signal and background. The diagonal line represents the performance of a random classifier with AUC=0.5.

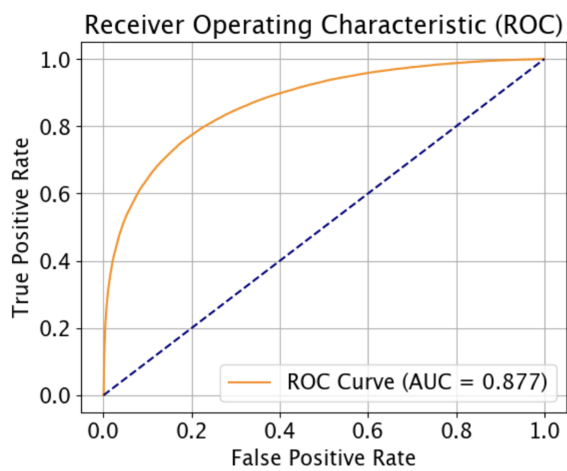


Figure 65: Receiver Operating Characteristic (ROC) curve for the FCNN model after feature engineering. The classifier achieves an area under the curve (AUC) of 0.877, indicating a stronger separation between signal and background. The diagonal line represents the performance of a random classifier with AUC=0.5.

## BIBLIOGRAPHY

- [1] S. Bifani, A. Hicheur, T. Rojo, and T. Blake, “Review of lepton universality tests in b decays,” *J. Phys. G*, vol. 46, no. 2, p. 023001, 2019.
- [2] Y. S. A. et al. (HFLAV Collaboration), “Averages of b-hadron, c-hadron, and  $\tau$ -lepton properties as of 2022,” *arXiv preprint*, 2022.
- [3] J. e. a. B. Lees, “Evidence for an excess of  $\bar{B} \rightarrow d^{(*)}\tau^{-}\bar{\nu}_{\tau}$  decays,” *Phys. Rev. D*, vol. 88, p. 072012, 2013.
- [4] M. e. a. B. Huschle, “Measurement of the branching ratio of  $\bar{B} \rightarrow d^{(*)}\tau^{-}\bar{\nu}_{\tau}$ ,” *Phys. Rev. D*, vol. 94, p. 072007, 2016.
- [5] R. Aaij et al., “Search for the decays  $b_s^0 \rightarrow \tau^+\tau^-$  and  $b^0 \rightarrow \tau^+\tau^-$ ,” *Phys. Rev. Lett.*, vol. 118, no. 25, p. 251802, 2017.
- [6] B. Bhattacharya, A. Datta, D. London, and S. Shivashankara, “Simultaneous explanation of the  $r_{K^{(*)}}$  and  $r_{D^{(*)}}$  puzzles: a model analysis,” *Phys. Lett. B*, vol. 773, pp. 256–263, 2017.
- [7] T. L. Collaboration, “The lhcb detector at the lhc,” *JINST*, vol. 3, p. S08005, 2008.
- [8] W. Altmannshofer et al., “The belle ii physics book,” *Prog. Theor. Exp. Phys.*, no. 12, p. 123C01, 2019.
- [9] S. Navas et al., “Review of particle physics,” *Phys. Rev. D*, vol. 110, no. 3, p. 030001, 2024.
- [10] L. Evans and P. Bryant, “LHC Machine,” *JINST*, vol. 3, p. S08001, 2008.
- [11] B. G. Siddi, “A fully parametric option in the LHCb simulation framework,” in *14th International Workshop on Top Quark Physics (TOP2019)*, ser. EPJ Web of Conferences, vol. 214. EDP Sciences, 2019, p. 02024. [Online]. Available: <https://doi.org/10.1051/epjconf/201921402024>
- [12] W. R. Leo, *Techniques for Nuclear and Particle Physics Experiments: A How-To Approach*, 2nd ed. Springer, 1994.
- [13] T. Sjöstrand, S. Mrenna, and P. Z. Skands, “A brief introduction to pythia 8.1,” *Comput. Phys. Commun.*, vol. 178, pp. 852–867, 2008.
- [14] D. J. Lange, “The evtgen particle decay simulation package,” *Nucl. Instrum. Meth. A*, vol. 462, pp. 152–155, 2001.
- [15] S. A. et al., “Geant4—a simulation toolkit,” *Nucl. Instrum. Meth. A*, vol. 506, no. 3, pp. 250–303, 2003.
- [16] T. Chen and C. Guestrin, “Xgboost: A scalable tree boosting system,” *Proceedings of the 22nd ACM SIGKDD International Conference on Knowledge Discovery and Data Mining (KDD)*, pp. 785–794, 2016.
- [17] V. R. Chippa, R. R. Singh, and A. V. Sathanur, “Energy-efficient classification for resource-constrained biomedical applications,” in *2018 IEEE Computer Society Annual Symposium on VLSI (ISVLSI)*, 2018, pp. 217–222.
- [18] A. D. Rasamoelina, F. Adjailia, and P. Sinčák, “A review of activation function for artificial neural network,” in *2020 IEEE 18th World Symposium on Applied Machine Intelligence and Informatics (SAMII)*, 2020, pp. 281–286.
- [19] X. Glorot, A. Bordes, and Y. Bengio, “Deep sparse rectifier neural networks,” in *Proceedings of the 14th International Conference on Artificial Intelligence and Statistics (AISTATS)*, 2011, pp. 315–323.
- [20] A. Semenov, V. Boginski, and E. L. Pasiliao, “Neural networks with multidimensional cross-entropy loss functions,” in *Computational Data and Social Networks*, ser. Lecture Notes in Computer Science, A. Tagarelli and H. Tong, Eds. Springer, Cham, 2019, vol. 11917, cSoNet 2019. [Online]. Available: [https://doi.org/10.1007/978-3-030-34980-6\\_5](https://doi.org/10.1007/978-3-030-34980-6_5)
- [21] D. P. Kingma and J. Ba, “Adam: A method for stochastic optimization,” *International Conference on Learning Representations (ICLR)*, 2015.
- [22] Particle Data Group, “Review of particle physics: Monte carlo numbering scheme,” <https://pdg.lbl.gov/2020/reviews/rpp2020-rev-monte-carlo-numbering.pdf>, 2020, accessed: 2025-03-23.
- [23] I. Goodfellow, Y. Bengio, and A. Courville, *Deep Learning*. MIT press, 2016.
- [24] M. Abadi, A. Agarwal, P. Barham, E. Brevdo, Z. Chen, C. Citro, G. S. Corrado, A. Davis, J. Dean, M. Devin, S. Ghemawat, I. Goodfellow, A. Harp, G. Irving, M. Isard, Y. Jia, R. Jozefowicz, L. Kaiser, M. Kudlur, J. Levenberg, D. Mané, R. Monga, S. Moore, D. Murray, C. Olah, M. Schuster, J. Shlens, B. Steiner, I. Sutskever, K. Talwar, P. Tucker, V. Vanhoucke, V. Vasudevan, F. Viégas, O. Vinyals, P. Warden, M. Wattenberg, M. Wicke, Y. Yu, and X. Zheng, “TensorFlow: Large-scale machine learning on heterogeneous systems,” <https://www.tensorflow.org/>, 2015, software available from tensorflow.org.
- [25] E. M. Aitala, S. Amato, J. C. Anjos, J. A. Appel, D. Ashery, S. Banerjee, I. Bediaga, G. Blaylock, S. B. Bracker, P. R. Burchat, R. A. Burnstein, T. Carter, H. S. Carvalho, N. K. Copty, L. M. Cremaldi, C. Darling, K. Denisenko, A. Fernandez, P. Gagnon, C. Gobel, K. Gounder, A. M. Halling, G. Herrera, G. Hurvits, C. James, P. A. Kasper, S. Kwan, D. C. Langs, J. Leslie, B. Lundberg, S. Maytal-Beck, B. Meadows, J. R. T. de Mello Neto, R. H. Milburn, J. M. de Miranda, A. Napier, A. Nguyen, A. B. d’Oliveira, K. O’Shaughnessy, K. C. Peng, L. P. Perera, M. V. Purohit, B. Quinn, S. Radeztsky, A. Rafatian, N. W. Reay, J. J. Reidy, A. C. dos Reis,

H. A. Rubin, A. K. S. Santha, A. F. S. Santoro, A. J. Schwartz, M. Sheaff, R. A. Sidwell, A. J. Slaughter, M. D. Sokoloff, N. R. Stanton, K. Stenson, D. J. Summers, S. Takach, K. Thorne, A. K. Tripathi, S. Watanabe, R. Weiss-Babai, J. Wiener, N. Witchey, E. Wolin, D. Yi, S. Yoshida, R. Zaliznyak, and C. Zhang, “Search for  $cp$  violation in charged  $d$  meson decays,” *Physics Letters B*, vol. 403, no. 3-4, pp. 377–382, 1997.

[26] J. P. Lees *et al.*, “Search for  $B^+ \rightarrow K^+ \tau^+ \tau^-$  at the BABAR experiment,” *Phys. Rev. Lett.*, vol. 118, no. 3, p. 031802, 2017.

[27] A. Dissertori, “Pseudorapidity and rapidity,” 2010, eTH Zürich Lecture Notes on Particle Physics, HS10, 2010. [Online]. Available: <https://edu.itp.phys.ethz.ch/hs10/ppp1/2010.11.02.pdf>

[28] R. Shwartz-Ziv and A. Armon, “Tabular data: Deep learning is not all you need,” *Advances in Neural Information Processing Systems*, vol. 35, pp. 26 383–26 398, 2022. [Online]. Available: <https://arxiv.org/abs/2106.03253>